Astrocytes mediate oxytocin's effect on central amygdala circuitry that regulates emotional behavior in rodents

Jérôme Wahis, Angel Baudon, Ferdinand Althammer, Damien Kerspern, Stéphanie Goyon, Daisuke Hagiwara, Arthur Lefevre, Lara Barteczko, Benjamin Boury-Jamot, Benjamin Bellanger, et al.

Astrocytes mediate oxytocin's effect on central amygdala circuitry that regulates emotional behavior in rodents

Jérôme Wahis[1,†,$], Angel Baudon[1,†], Ferdinand Althammer[2,†], Damien Kerspern[1,†], Stéphanie Goyon[1], Daisuke Hagiwara[3], Arthur Lefevre[1,3], Lara Barteczko[3], Benjamin Boury-Jamot[4], Benjamin Bellanger[1], Marios Abatis[4], Miriam Silva da Gouveia[5], Diego Benusiglio[3], Marina Eliava[3], Andrej Rozov[6], Ivan Weinsanto[1], Hanna Sophie Knobloch-Bollmann[7,$], Matthew K. Kirchner[2], Ranjan K. Roy[2], Hong Wang[8,$], Marie Pertin[9], Perrine Inquimbert[1], Claudia Pitzer[10], Jan Siemens[8], Yannick Goumon[1], Benjamin Boutrel[4], Christophe Maurice Lamy[11], Isabelle Decosterd[9,12], Jean-Yves Chatton[9], Nathalie Rouach[13], Scott W. Young[14], Javier E. Stern[2], Pierrick Poisbeau[1], Ron Stoop[4], Pascal Darbon[1], Valery Grinevich[3,#,*], Alexandre Charlet[1,15,#,*]

[1] Centre National de la Recherche Scientifique and University of Strasbourg, UPR3212 Institute of Cellular and Integrative Neurosciences, Strasbourg, France. [2] Center for Neuroinflammation and Cardiometabolic Diseases, Georgia State University, Atlanta, USA. [3] Department of Neuropeptide Research for Psychiatry, Central Institute of Mental Health, University of Heidelberg, Mannheim, Germany. [4] Center for Psychiatric Neurosciences, Hôpital de Cery, Lausanne University Hospital (CHUV), Lausanne, Switzerland. [5] German Cancer Research Center (DKFZ), Heidelberg, Germany, [6] OpenLab of Neurobiology, Kazan Federal University, Kazan, Russia, Federal Center of Brain Research and Neurotechnologies, Moscow, Russia and Department of Physiology and Pathophysiology, University of Heidelberg, Heidelberg, Germany. [7] Department of Molecular and Cellular Biology, Center for Brain Science, Harvard University, Cambridge, USA[$]. [8] Department of Pharmacology, Heidelberg University, Heidelberg, Germany[$]. [9] Pain center, Department of Anesthesiology, Lausanne University Hospital (CHUV), Lausanne, Switzerland. [10] Interdisciplinary Neurobehavioral Core (INBC), Ruprecht-Karls-Universität, Heidelberg. [11] Division of Anatomy, Faculty of Medicine, University of Geneva, Geneva, Switzerland. [12] Department of Fundamental Neurosciences, Faculty of Biology and Medicine (FBM), University of Lausanne, Lausanne, Switzerland. [13] Neuroglial Interactions in Cerebral Physiopathology, Center for Interdisciplinary Research in Biology, Collège de France, Centre National de la Recherche Scientifique UMR 7241, Institut National de la Santé et de la Recherche Médicale U1050, Labex Memolife, PSL Research University, Paris, France. [14] Section on Neural Gene Expression, National Institute of Mental Health, National Institutes of Health, Bethesda, MD, USA. [15] University of Strasbourg Institute for Advanced Study (USIAS), Strasbourg, France. [$]Present addresses: JW: Laboratory of Glia Biology, VIB-KU Leuven Center for Brain and Disease Research, Department of Neuroscience, KU Leuven Brain Institute, Leuven, Belgium. HSKB: Group of Systemic and Cellular Neuroscience, Institute of Physiology, University of Freiburg, Germany. HW: The Brain Cognition and Brain Disease Institute of Shenzhen Institutes of Advanced Technology, Chinese Academy of Sciences, China.

[†] Equal first author. [#] senior author. * Corresponding author.

Corresponding Authors

Alexandre Charlet, PhD
Institute of Cellular and Integrative Neurosciences,
INCI CNRS UPR3212

8, Allée du Général Rouvillois
67000 Strasbourg
France
Phone: (33) 6070 825 06
E-mail: acharlet@unistra.fr

Valery Grinevich, MD, PhD
Department of Neuropeptide Research in Psychiatry
Central Institute of Mental Health
Medical Faculty Mannheim
University of Heidelberg
J5, Mannheim, 68159
Germany
Phone: (49) 621 1703 2995
E-mail: valery.grinevich@zi-mannheim.de

SUMMARY

Oxytocin (OT) orchestrates social and emotional behaviors through modulation of neural circuits. In the central amygdala (CeA), the release of OT modulates inhibitory circuits and thereby suppresses fear responses and decreases anxiety levels. Using astrocyte-specific gain- and loss-of-function and pharmacological approaches, we demonstrate that a morphologically distinct subpopulation of astrocytes express OT receptors and mediate anxiolytic and positive reinforcement effects of OT in the CeA of mice and rats. The involvement of astrocytes in OT signaling challenges the long-held dogma that OT acts exclusively on neurons and highlight astrocytes as essential components for modulation of emotional states under normal but also chronic pain conditions.

INTRODUCTION

Oxytocin (OT) is a neuropeptide that acts both as a peripheral neurohormone and a central neuromodulator to modulate key physiological functions, from ion homeostasis to complex social behaviors[1,2]. Early studies indicated that locally released OT induces morphological and functional changes in both the astroglial and neuronal networks of the hypothalamic nuclei producing the neuropeptide[3]. Activation of oxytocinergic hypothalamic magnocellular neurons, that project further to virtually all forebrain regions, leads to both synaptic and extra-synaptic OT release in the extra-cellular fluid[4,5]. This last mode of OT release has the potential to activate virtually every cell type expressing OT receptors (OTR) located in close proximity to the sites of axonal OT release[5].

A few studies using either autoradiography on cell cultures derived from rat tissue, immunohistochemistry on CNS sections or knock-in mice models found that not only neurons, but also astrocytes express OTRs[6–9]. Astrocytes are part of the tripartite synapse

and capable to modulate neuronal activity as well as to sense the release of neuromodulators into the neuropil[10]. There is now accumulating evidence which demonstrate that astrocytes express receptors for various neuromodulators and actually mediate their neurophysiological effects[11,12]. Mapping of OTR expression in the rodent brain found it was expressed at high levels in several brain regions[8], and of interest in this study particularly in the lateral and capsular part (CeL) of the central amygdala (CeA)[13], albeit the types of cells expressing the OTR in this brain region was never elucidated.

Functionally, the release of OT in the CeL leads to increased firing of GABA-expressing interneurons[4,13]. These interneurons inhibit projection neurons in the medial CeA (CeM), which serve as CeA output. OT action in this circuit affects amygdala-related functions, including activity of the autonomous nervous system, fear expression and anxious behaviors[4,14,15]. Furthermore, the CeA is involved in the pathophysiology of a number of neurological diseases, including neuropathic pain and anxiety[16,17], in which both astrocytes[18] and the OT system[19] are thought to play a significant role. Therefore, it is crucial to understand how the OT system controls pain and its emotional comorbidities, and if astrocytes are involved in these mechanisms.

Indeed, a role for astrocytes in the regulation of CeA circuits has already been proven in the CeM[20], where astrocyte activity can reduce fear-expression in a fear-conditioning paradigm, a role that is surprisingly similar to the effect of OTR signaling in the CeL[4]. We therefore sought to investigate if CeL astrocytes could also play a role in the OT-mediated regulation of CeA circuits and some of their behavioral correlates.

Our study shows the expression of oxytocin receptors (OTR) in CeL astrocytes and demonstrates that OT directly acts on CeL astrocytes to gate CeL neurons excitability through N-methyl-D-aspartate receptor (NMDAR) (co-)activation. Further, we found that the astrocyte-mediated OTR signaling underlies the anxiolytic and positive reinforcement effects of OT in the CeA. We thus provide the first evidence that OT drives astrocyte activity and that this effect is an essential part of the OTergic modulation of amygdala neuronal circuits and the behaviors they regulate.

RESULTS

CeL astrocytes express functional OTRs in rats and mice

To investigate whether CeA astrocytes express OTRs, we performed fluorescent *in situ* hybridization (FISH) combined with immunohistochemistry on rat CeA sections and found some overlap between OTR mRNA signal and an astrocyte marker, glutamine synthase (GS) (Fig. 1a-b; Extended Data Fig. 1a). Within the rat CeL, 18.6±1.8% of astrocytes and 67.8±3.1% of neurons expressed OTR mRNA (Fig. 1c), with similar results in mice (Extended Data Fig. 1b). Using another astrocyte marker, the aldehyde dehydrogenase 1 family member L1 (ALDH1L1), we found a similar proportion of OTR mRNA positive (OTR+) rat astrocytes (Extended Data Fig. 1c). Combining RNAscope for OTR mRNA with a third astrocyte marker (glial fibrillary acidic protein, GFAP), we again found OTR mRNA to be present in mouse astrocytes (Extended Data Fig. 1d). Next, to unequivocally demonstrate that CeL astrocytes were positive for OTR, we employed IHC-based three-dimensional reconstruction using Imaris technique and combining immunohistochemical staining for GS and GFAP with FISH for OTR mRNA in the rat CeL. Employing glial morphometric profiler, we performed three-dimensional reconstruction of cells through a semi-automated pipeline[21] (Fig. 1d-e). This analysis confirmed the presence of OTR mRNA in astrocytes and revealed that OTR+ astrocytes have on average a significantly larger cell volume, surface area, a higher number and an increased length of processes compared to OTR– astrocytes (Fig. 1e). Subsequent Sholl analysis revealed that OTR+ astrocytes bear more complex morphological features than OTR– astrocytes (Fig. 1f), suggesting that OTR+ astrocytes represent a distinct subpopulation of astrocytes within the CeL.

To test whether CeL astrocytes respond to endogenous OT release, we expressed the ChR1/VChR1 chimaera channel rhodopsin variant[22] (referred here as C1V1) in OTergic neurons to optogenetically control CeA-innervating OT axons (POT-C1V1-mCherry; referred to as OxytOpto). To this end, we employed a previously characterized adeno-associated viral vector (AAV) equipped with the OT promoter[4], which was injected into the paraventricular (PVN), supraoptic, and accessory nuclei of rat hypothalamus (Fig. 2a). First, we validated that red shifted light (λ542 nm light pulses of 10 ms width at 30 Hz) induced activation of C1V1-expressing OT neurons in the PVN (Extended Data Fig. 2a-b). We then identified CeL astrocytes through sulforhodamine 101 (SR101) labeling in acute brain slices and confirmed astrocytes specificity of the labeling by measuring electrophysiological properties of SR101-labelled cells in CeL (Extended Data Fig. 2c-e). We then assessed SR101 labeled astrocytes activity by measuring the relative changes in cytosolic calcium using the small organic dye Oregon Green® 488 BAPTA-1 (OGB1). (Fig. 2b). We found that of recorded astrocytes, 61.9±8.7% responded to the optogenetic OT axons stimulation (Fig. 2c-d). To avoid the possibility that astrocyte activity was increased due to the increased spiking of CeL interneurons caused by optogenetically evoked OT release, tetrodotoxin (TTX) was added to the bath prior the stimulation. Further calcium imaging experiments described below use TTX incubation (if not stated otherwise) for the same reason,. We also compared the frequency of calcium transients as well as the area under the curve before and after optogenetic stimulation, expressing the results as a ratio between post-stimulation and baseline values (referred to as AUC and Ca^{2+} transient frequency normalized to baseline,

analysis method detailed in Extended Data Fig. 2f). As depicted in Fig. 2d, both parameters were increased following stimulation of OT axons. Taken together, these results indicate that optogenetically-evoked OT release from axons present in the CeL elicits an increase in activity of CeL astrocytes.

To ensure that the observed responses are exclusively due to OTR activation, we applied the selective agonist of OTR ([Thr^{4}Gly^7]-oxytocin, TGOT), which increased calcium transients in 60.1±9.2% of the recorded astrocytes, a result unchanged when replicated with slices pre-incubated with TTX (Fig. 2e-f). Similar pre-incubation of the slices with the OTR antagonist [d(CH$_2$)^5,Tyr(Me)^2,Orn^8]-vasotocin (dOVT) reduced the proportion of TGOT-evoked calcium responses in astrocytes and their properties (Fig. 2e-f), confirming that the activation of astrocytes by TGOT is indeed mediated by OTR. However, it cannot be discarded that other OTR-mediated and astrocyte-independent mechanisms may drive CeL astrocyte activity up.

To exclude this possibility, we employed a transgenic mouse line with a LoxP sites flanking the OTR gene[23] (OTR cKO mice). To specifically delete OTRs in astrocytes, we injected an AAV driving expression of Cre recombinase under the control of the GFAP promoter in the CeL (P$_{GFAP}$-Cre, Fig. 2g). This led to to expression of Cre in 56.0±4.9% of astrocytes within the injection site, with a specificity reaching 96.2±2.1% (Extended Data Fig. 2g). P$_{GFAP}$-Cre AAV injection in OTR cKO mice resulted in a drastic decrease in OTR mRNA signal in astrocytes (Fig 2h), but not in neurons (Extended Data Fig. 2h). Similarly to results obtained in rats, TGOT application in TTX-treated acute slices of the CeL from control mice led to responses in 43.9±7.2% of astrocytes (Fig. 2i), whereas these responses were largely reduced in CeL astrocytes from P$_{GFAP}$-Cre AAV injected OTR cKO mice (GFAP OTR KO, Fig. 2i). These results confirm that astrocytes respond directly to OTR activation independently from TGOT effects on CeL neurons.

Activation of OTR+ astrocytes propagates through an astrocyte network

Since astrocytes are known to form extensive intercellular networks, we next studied the spatial connectivity of OTR+ astrocytes in the CeL. (Fig. 3a, Extended Data Fig. 3a). We found that the distance between OTR+ astrocyte pairs (95.8±4.0µm) was larger than the distance between OTR- astrocyte pairs (37.4±0.9µm, Fig. 3a). In addition, we found that OTR+ astrocytes had significantly more contacts with OTR-, than with OTR+ astrocytes (Fig. 3a), whereas OTR- regularly contact other OTR- astrocytes (3.7±1.3 contacts).

These anatomical results suggest a specific distribution pattern of OTR+ astrocytes within the CeL, where OTR+ astrocytes are found distant from their counterparts and exhibit numerous connections with others, OTR- astrocytes. Interestingly, the proportion of rats and mice astrocytes responsive to OTR activation always exceeded 40% of recorded cells (Fig. 2) despite our FISH/Imaris results indicating that less than 20% of astrocytes expressed OTRs mRNA (Fig. 1). This apparent discrepancy led us to test whether the minor population of OTR+ astrocytes could spread their activation following OTR signaling to a much larger population of OTR- astrocytes.

There are two common signaling pathways typical for astrocytes which could facilitate the spread of activation from OTR+ to OTR- astrocytes: (i) paracrine purinergic communication and (ii) gap-junctions mediated spread of activity. To decipher the underlying mechanism, we

first blocked purinergic receptors using pyridoxalphosphate-6-azophenyl-2',4'-disulfonic acid (PPADS) and found that this blocker did not significantly affect the average proportion of astrocytes activated by TGOT (Fig. 3b), nor the properties of these responses (Fig. 3b), a result replicated using a set of purinergic receptors antagonists blocking the majority of known purinergic receptors (Extended Data Fig. 3b-c). Yet, the incubation with the gap-junctions blocker carbenoxolone (CBX) significantly reduced the number of astrocytes responsive to TGOT+TTX application (Fig. 3b). Given that astrocyte gap-junctions are primarily composed of the connexins (Cx) 30 and 43, we further tested their involvement in OTR-induced signal spreading by using a Cx30/Cx43 double KO mice line, previously shown to lack astrocyte gap junctional communication[24] (Fig. 3c). As found with CBX, the number of astrocytes activated by TGOT was significantly reduced in these mice (Fig. 3c). These results indicate that gap junctions play a role in the propagation of responses following OTR activation in the CeL astrocytes network, possibly from OTR+ to OTR- astrocytes. This is corroborated by the anatomical observations that biocytin infused in the cytosol of astrocytes spread from one cell to another within the CeL network at least in part via gap-junctions (Fig. 4e).

CeL astrocyte activity increases CeL neurons excitability

We next wanted to test if this direct astrocyte network response to OTR activation could be relevant to the known effect of OTR signaling on CeA neuronal networks [4,13,14]. To manipulate astrocytic activity, we expressed the opsin C1V1 under the control of the GFAP promoter using rAAV injections (P_{GFAP}-C1V1-mCherry; referred to as AstrOpto, Fig. 4a). After confirmation of vector expression in 62.5±3.1% of all astrocytes in the CeL, with a specificity reaching 98.8±0.7% (Extended Data Fig. 4a), we evaluated the effect of C1V1 stimulation on astrocyte calcium activity (Fig. 4b). We observed responses in 60.8±9.0% of astrocytes (Fig. 4c), a proportion comparable to what we observed following OTR stimulation by TGOT+TTX (AstrOpto vs TGOT+TTX: p = 0.8265, unpaired t-test). The removal of extracellular calcium prevented the C1V1-driven astrocyte activity (Extended Data Fig. 4b). This indicates that influx of extracellular calcium through the plasma membrane is required to generate calcium transient activity in astrocytes following C1V1 activation (Extended Data Fig. 4b).

Next, we measured the effect of evoked astrocyte activity, using AstrOpto or direct OTR stimulation through TGOT application, on CeL neurons excitability measured through patch-clamp techniques. Optical stimulation of C1V1 in astrocytes increased the frequency of miniature excitatory post-synaptic currents (mEPSCs) in CeL neurons (Fig. 4d) while bath-applied TGOT had a similar effect (Fig. 4f). We next infused BAPTA specifically in the astrocyte network (Fig. 4e) to block the increase in calcium transients evoked by TGOT, and found it also blocked TGOT effect on CeL neurons mEPSCs (Fig. 4e-f). This indicates that OTR activation and the ensuing increased in calcium transients in astrocytes is driving up excitatory inputs to CeL neurons.

To identify the intercellular communication pathway involved in astrocytes-neurons communication following OTR-dependent activation of astrocytes, we studied whether N-Methyl-D-Aspartate receptor (NMDAR), a well-known neuronal receptor that can be activated

by astrocytic gliotransmission[12,25,26], was involved. Thus, we applied a NMDAR antagonist (2R)-amino-5-phosphonovaleric acid (AP5) prior to TGOT application and found it inhibited TGOT effect on mEPSCs frequency (Fig. 4f). Importantly, AP5 had no effect on astrocyte responses to TGOT, thereby excluding the involvement of NMDAR in CeL astrocytes responses to TGOT (Extended Data Fig. 3d). Finally, to unambiguously demonstrate that astrocytes underlie the effect of OTR signaling on CeL neuron excitatory synaptic transmission, we repeated the mEPSCs measurements in control and GFAP OTR KO mice. TGOT application increased mEPSCs frequency in control mice, but not in GFAP OTR KO mice (Fig. 4g-h), confirming the role of astrocytic OTR in mediating the effects of OTR signaling on synaptic inputs in CeL neurons.

We then investigated whether the increase in mEPSCs frequency in CeL neurons following OTR activation was able to increase their firing frequency. To address this question, we applied the same stimulation protocols as before, and subsequently recorded spontaneous action potential (AP) firing (Fig. 5a-b). First, AstrOpto increased firing of CeL neurons, an effect that was blocked by previous infusion of BAPTA in the astroglial network, hence proving its dependence on astrocyte calcium signaling (Fig. 5c). Similarly, and in agreement with its effect on CeL neurons mEPSC, TGOT also increased neuronal spiking activity (Fig. 5d), an effect which was abolished following either BAPTA infusion in the astroglial network or pre-incubation of AP5 in the recording bath (Fig. 5d). Crucially, TGOT application increased the firing of CeL neurons in control but not in GFAP OTR KO mice (Fig. 5e-f).

These results unequivocally demonstrate that OTR signaling in the CeL requires the expression and activation of OTR and its associated calcium signaling in astrocytes, which further lead to an increase in the excitability of CeL interneurons through NMDAR-dependent mechanisms.

CeL astrocytes activity increases inhibitory inputs onto CeM projection neurons

Previous work showed that the activation of CeL OTRs leads to an increased activity of GABAergic CeL neurons, a result we replicated here (Fig. 5). A demonstrated direct consequence of this is an increased frequency of $GABA_A$-mediated inhibitory post-synaptic currents (IPSCs) in CeM projection neurons[4,13,14].

In agreement with these findings, we found that optogenetic activation of CeL astrocytes (through AstrOpto) evoked an increase in IPSC frequency in rat CeM neurons (Fig. 6a-c). This effect was also dependent on CeL astrocytic calcium signaling, as BAPTA infusion in CeL astrocytes abolished it (Fig. 6c). Furthermore, the effect of AstrOpto on CeM IPSCs frequency was suppressed by application of AP5, but also by prior degradation of D-serine (an NMDAR co-agonist) with D-amino acid oxidase (DAAO) (Extended Data Fig. 5a). D-Serine is a known gliotransmitters, whose levels have been found to be increased following astrocytic GPCR activation[27]. Altogether, these results indicate that the effect of AstrOpto on IPSCs in CeM neurons is dependent on the activation of NMDARs in CeL neurons. TGOT application produced a similar effect on CeM neurons, also dependent on CeL astrocytic calcium signaling (Fig. 6d) and on NMDARs (Fig. 6d). Initial incubation with DAAO similarly blocked the effect of TGOT on IPSCs frequency (Extended Data Fig. 5b). Crucially, D-serine supplementation in the DAAO-treated slices following the first, effectless, TGOT application rescued the effect of a second TGOT application on IPSCs frequency (Extended Data Fig.

5b-d). This confirms the involvement of neuronal NMDARs and its co-agonist D-Serine in OTR-mediated modulation of CeA neuronal network. To further complement these results, we found that bath application of 5,7-dichlorokynurenic acid (DCKA), a potent antagonist of the NMDAR glycine/D-Serine modulatory site, also abolished TGOT effects on CeM IPSC frequency, while the AMPAR antagonist DNQX had no effect (Extended Data Fig. 5e). In addition, pre-incubation with the purinergic receptors antagonists PPADS, CPT or SCH 58261 had no effects either (Extended Data Fig. 5f). This confirms that the primary mode of astrocyte to neuron communication engaged following OTR signaling in CeA involves NMDARs, but not purinergic signaling in neurons, and is mediated by an increase in D-serine levels.

As in rats, TGOT application also led to an increased IPSC frequency in CeM neurons in brain slices from control mice, but not in slices from GFAP OTR KO mice (Fig. 6e-f). These *ex vivo* results clearly demonstrate that direct of OTR-mediated CeL astrocytes activation leads to an NMDAR-dependent increase in CeL neurons excitability, which further increases inhibitory inputs into CeM projection neurons.

Our data so far demonstrate that when OTR signaling is engaged in astrocytes, these cells increase the excitability of CeL neurons, directly leading to an increase in inhibitory inputs into CeM projection neurons. Altogether, these results demonstrate that the effect of OT on neuronal activity is abolished when astrocyte function is compromised, establishing for the first time that OT signaling in CeA circuitry is locally transduced by astrocytes.

OTR signaling through astrocytes is crucial for emotional balance regulation.

The CeA is a key nucleus for the processing of emotional information, and notably plays an important role in pain-associated disorders[16], for which OT has been demonstrated as a crucial regulator[19]. We therefore chose to first test the involvement of OTR-mediated (or direct) astrocyte activation in modulating mechanical pain hypersensitivity (Fig. 7b,f), levels of anxiety (Fig. 7c,g), and reinforcement behavior (Fig. 7f,h) in rats and mice that developed neuropathic pain and the associated increased anxiety following a spared nerve injury (SNI) surgery[28] (Extended Data Fig. 6a).

Given that there is a proven link between chronic pain etiology and synaptic changes in the CeA[29], we initially tested whether the effect of TGOT on astrocytes calcium signaling and CeM neurons IPSCs frequency was altered in SNI rats, but did not find any differences compared to sham-operated animals (Extended Data Fig. 6b-c). This indicates that OTR signaling in CeA, at least at the levels of the circuit studied here, is unaltered in SNI animals. We further confirmed that D-Serine was still required for TGOT effects in the CeA of SNI animals using DAAO pre-incubation followed by exogenous D-Serine supplementation in the *ex vivo* setting (Extended Data Fig. 6d).

Following our finding that SNI procedure did not alter the effect of TGOT at the circuit level, we next used a nociceptive assay to measure the mechanical threshold for paw withdrawal in both rats and mice. We found that SNI animals displayed a decreased mechanical threshold, but bilateral micro-injections of TGOT in the CeA had no clear effect on it, with only a mild anti-nociceptive effect only in rats (Fig. 7b,f). Moreover, bilateral optogenetic stimulation of

rats CeL astrocytes (AstrOpto) had no noticeable effect on mechanical threshold in rats (Fig. 7b; Extended Data Fig. 7b).

Next we performed an elevated plus maze (EPM) test, and found that SNI animals spent significantly more time in the closed arm compared to sham-operated ones, indicating the SNI procedure induced a state of elevated anxiety (Fig. 7c,g) as expected. When TGOT was injected in CeA, time spent in the closed arm was significantly reduced to levels comparable to those observed in sham animals, indicating an anxiolytic effect of OTR signaling in both rats and mice (Fig. 7c,g). Crucially, AstrOpto in rats had a comparable effect (Fig. 7c), while the deletion of OTR from CeL astrocytes in mice abolished the anxiolytic effects of TGOT (Fig. 7g), highlighting the involvement of astrocytic OTRs also at the behavioral level. Interestingly, sham mice with deletion of OTR in CeL astrocytes displayed an anxious behavior (Fig. 7g), which indicates OTR signaling through astrocytes is involved in emotional balance, even under pain-free conditions.

In order to further investigate the role of the CeA in attributing emotional valence to stimuli, we used the conditioned place preference (CPP) test in rats and mice that underwent an SNI or sham procedures. Here, both SNI and sham animals exhibited a clear preference for the chamber paired with TGOT infusion (Fig. 7d,h). The optogenetic activation of astrocytes in rat CeL also led to a place preference, mimicking TGOT action (Fig. 7d), while TGOT lost its positive conditioning effects in GFAP OTR KO mice (Fig. 7h). Importantly, neither the treatments nor the SNI procedure significantly affected the motor activity of rats and mice in both the EPM or CPP tests (Extended Data Fig. 7).

Collectively, our findings demonstrate from the local circuit to the behavioral levels that OTR signaling through CeL astrocytes is a novel and important mechanism involved in emotional states regulation, this under both normal and chronic pain conditions (Fig. 7i).

DISCUSSION

We here demonstrate that OTR signaling through astrocytes is crucial for the oxytocinergic modulation of the local CeA microcircuit and its behavioral correlates. We further propose that this effect relies on a morphologically defined subpopulation of OTR+ astrocytes (Fig. 1-2), that convey their activation by OT to other astrocytes through gap-junctional communication (Fig. 3), leading to an increase in activity in the majority of CeL astrocytes (Fig. 2-3). In turn, astrocytes increase the excitability of CeL interneurons by gating activation of NMDA receptors (Fig. 4-5), leading to an increase in GABAergic inhibitory inputs in post-synaptic neurons located in the CeM (Fig. 6). At the behavioral level, this OTR-mediated modulation of CeA astro-neuronal network promotes a positive emotional state, measured as clear anxiolytic and positive reinforcement effects (Fig. 7).

Mechanistically, our results reinforce previous demonstrations of a role of astrocytes in transforming neuromodulators signaling into a change in the gain of neuronal circuits, notably by (co-)activating neuronal NMDAR[12,25,26]. Despite the high proportion of OTR+ neurons (up to 70%) compared to the limited number of OTR+ astrocytes (~18%) in the CeL, the activation of OTRs in astrocytes was required to gate CeL neurons responses to OTR activation by allowing a sustained (co)activation of NMDARs. Other mechanisms are probably at play: OTR activation in CeL neurons might inhibit K+ leak current, as has been shown in olfactory neuronal cells[30] and in spinal cord[31]. These mechanisms might act in synergy to induce an elevation in firing rates of CeL neurons by increasing the gain of excitatory inputs in these cells. Furthermore, similar mechanisms of astrocytes to neuron communication through neuronal NMDARs (co)activation have been proposed by other studies to favor a synchronous increase in excitability across an ensemble of neurons[32,33]. This would allow a synchronized and long-lasting switch in the gain of the CeA neuronal circuits, thereby amplifying the effect of OT on CeA outputs in both the spatial and temporal domains. In light of the predominantly non-synaptic mode of OT release from axons *en passant*, which could lead to CeL-restricted micro-volume transmission of the neuropeptide[5], it seems then plausible that astrocytes are required to relay and amplify OT signaling to CeL neurons. Another mechanism that was repeatedly found to be involved in neuromodulators signaling through astrocytes is the activation of purinergic signaling in neurons[34,35]. However, in the case of OT signaling within the CeA, purinergic signaling was not involved (Extended Data Fig. 5). It would then be interesting to test if astrocytes are important to OT signaling in other brain regions, and if they are, if the same mechanisms of astrocytes to neurons communication are at stake.

We found that CeA astrocytes can be divided into two defined populations: OTR+ and OTR- astrocytes. OTR+ astrocytes are morphologically more complex and have more close contacts with neighboring, OTR- astrocytes, while being quite distant from their OTR+ counterparts with whom they have almost no contacts (Fig. 1, 2). Thus, we hypothesize that these morphological peculiarities allow the propagation of OTR evoked calcium transients (Fig. 2) to a much larger number of OTR- astrocytes through, at least partially, gap junctions (Fig. 3b-c). Therefore only a few, strategically positioned OTR+ astrocytes are sufficient to result in a network wide effect of OT release in the CeL, despite the relatively moderate number of OT fibers found in this nucleus[4]. By describing a new population of astrocytes, our

work add to the recent advances in describing molecular, morphological and functional heterogeneity in astrocytes population[36,37] and opens up new perspectives into understanding how astrocytes subpopulations are functionally organized and communicate inside CNS circuits.

OT and its effects on brain circuits, and ultimately behavior, are under intense scrutiny, from fundamental research in animal models to behavioral and physiological studies in humans[38,39]. Among other roles, OT is considered a powerful anxiolytic peptide through its action in the human amygdala[40]. Yet, all studies so far considered as an accomplished fact that OT was acting directly on neurons, despite the controversies regarding the cellular substrates of BOLD fMRI signals often used in human studies, with some results arguing for a major contribution of astrocyte activity to these signals[41,42]. Furthermore, a significant number of studies demonstrated that astrocytes or their invertebrates counterparts are key, if not primary, targets of neuromodulators[12,25,26,34,35,43], and that astrocytes might be the causal elements behind shifts in brain states[11,43,44], a function usually attributed mainly to neuromodulators direct action on neurons[45]. Thus, further research focused on astrocytes-mediated modulation of human brain circuits' activities is particularly promising to develop refined strategies for future therapeutic approaches. Indeed, neuromodulators are the targets of numerous, already available, treatments of psychiatric diseases using either small molecule drugs or electrical stimulation protocols, such as deep brain[46] or transcranial stimulations[47], for which astrocytes also seem particularly involved[46,47]. Taken together, this indicates a need for a more global and systematic consideration of astrocytes roles in brain circuits, notably regarding the effect of neuromodulators, and in particular OT. We believe this is especially relevant for the development of better therapeutics in the field of chronic pain, which imposes a massive burden to society, impacting ~20% of the global population[48].

Indeed, considering that general anxiety and depression are frequent comorbidity of chronic pain[49], our finding that the activation of OT signaling in CeL astrocytes promotes a form of emotional comfort by alleviating anxious behavior and has positive reinforcement properties is promising: it demonstrates that activation of a particular, astrocyte-mediated, OTR pathways affect one of the most impactful aspect of the chronic pain sphere, the emotional one. This further highlights astrocytes as important cellular substrates of emotional regulation, which several studies have also argued for (see[50] and references therein). In this context, targeting the OT system and/or astrocytes specifically, in the amygdala or other CNS regions, might lead to the development of new therapeutic avenues to improve patient's well-being.

ACKNOWLEDGEMENTS

This work was supported by the IASP Early Career Research grant 2012, FP7 Career Integration grant 334455, Initiative of Excellence (IDEX) Attractiveness grant 2013, IDEX Interdisciplinary grant 2015, University of Strasbourg Institute for Advanced Study (USIAS) fellowship 2014-15, Foundation Fyssen research grant 2015, NARSAD Young Investigator Grant 24821, ANR JCJC grant (to AC); ANR-DFG grant GR 3619/701 (to AC and VG); Alexander von Humboldt fellowship (to DH), Seed grant from DFG within the Collaborative center SFB 1158 and Fyssen Foundation fellowship (to AL), DFG grants GR 3619/13-1 and GR 3619/16-1 (to VG), SFB 1158 (to CP, JS, and VG); SNSF-DFG grant GR 3619/8-1 (to RS and VG), Fritz Thyssen foundation (to VG); DFG Postdoc Fellowship AL 2466/1-1 to FA, Alexander von Humboldt Foundation (to DH); Fyssen foundation and PROCOP grant and SFB1158 seed grant for young scientists (to AL); Research Foundation - Flanders, fellowship (12V7519N) (to JW); Russian Science Foundation RSF (17-75-10061) and the Subsidy Allocated to the Kazan Federal University for the State Assignment № 0671-2020-0059 (to AR); the intramural research program of the NIMH (ZIAMH002498) (to WSY); National Institutes of Health grants R01NS094640 and R01HL090948 (to JES). European Research Council (Consolidator grant #683154) and European Union's Horizon 2020 research and innovation program (Marie Sklodowska-Curie Innovative Training Networks, grant #722053, EU-GliaPhD) (to NR). The authors thank Vincent Lelièvre for *in situ* hybridization advices; Romain Goutagny for *in vivo* optogenetics assistance; Fulvio Magara for anxiety behavior advices; Barbara Kurpiers and the Interdisciplinary Neurobehavioral Core Facility of Heidelberg University for experiments performed there; Sophie Reibel and the Chronobiotron UMS 3415 for all animal care; Thomas Splettstoesser (www.scistyle.com) for the help with the preparation of figure 7.

AUTHOR CONTRIBUTIONS

Conceptualization, AC; Methodology, AC, BBo, CML, CP, DK, FA, ID, JES, JW, JYC, NR, PD, PP, RS, VG, WSY, YG; Analysis, AC, BBe, BBJ, CML, DK, FA, HSKB, JW, SG; *In situ* hybridization, DH, FA, HSKB, HW, JS, ME; Immunohistochemistry, AL, DH, FA, JW, ME, MdSG; Imaris analysis: FA, MKK, RKR; *Ex vivo* patch-clamp electrophysiology, AB, AC, JW, SG, DK, IW, BBe, MA; *Ex vivo* calcium imaging, AB, CML, DK, JW; Astrocytes characterization, AB, AR, BBe, DK, IW, ME, SG; Behavior, AC, BBJ, DK, JW; Mice line validation, WSY; Viral vectors validation, MdSG, ME, VG; Spared nerve injuries, PI, MP; Writing, AB, AC, DK, FA, JW, VG; Funding acquisition AC, VG; Supervision, AC, VG; Project administration, AC.

DECLARATION OF INTERESTS

The authors declare no competing interest

REFERENCES

1. Lee, H.-J., Macbeth, A. H., Pagani, J. H. & Young, W. S. Oxytocin: the great facilitator of life. *Prog. Neurobiol.* **88**, 127–51 (2009).
2. Gimpl, G. & Fahrenholz, F. The oxytocin receptor system: structure, function, and regulation. *Physiol. Rev.* **81**, 629–83 (2001).
3. Theodosis, D. T. Oxytocin-secreting neurons: A physiological model of morphological neuronal and glial plasticity in the adult hypothalamus. *Front. Neuroendocrinol.* **23**, 101–35 (2002).
4. Knobloch, H. S. *et al.* Evoked axonal oxytocin release in the central amygdala attenuates fear response. *Neuron* **73**, 553–66 (2012).
5. Chini, B., Verhage, M. & Grinevich, V. The Action Radius of Oxytocin Release in the Mammalian CNS: From Single Vesicles to Behavior. *Trends Pharmacol. Sci.* **38**, 982–991 (2017).
6. Kuo, J., Hariri, O. R. & Micevych, P. An interaction of oxytocin receptors with metabotropic glutamate receptors in hypothalamic astrocytes. *J. Neuroendocrinol.* **21**, 1001–6 (2009).
7. Wang, P., Qin, D. & Wang, Y.-F. Oxytocin Rapidly Changes Astrocytic GFAP Plasticity by Differentially Modulating the Expressions of pERK 1/2 and Protein Kinase A. *Front. Mol. Neurosci.* **10**, 1–14 (2017).
8. Mitre, M. *et al.* A Distributed Network for Social Cognition Enriched for Oxytocin Receptors. *J. Neurosci.* **36**, 2517–2535 (2016).
9. Yoshida, M. *et al.* Evidence that oxytocin exerts anxiolytic effects via oxytocin receptor expressed in serotonergic neurons in mice. *J. Neurosci.* **29**, 2259–71 (2009).
10. Hirase, H., Iwai, Y., Takata, N., Shinohara, Y. & Mishima, T. Volume transmission signalling via astrocytes. *Philos. Trans. R. Soc. B Biol. Sci.* **369**, 20130604–20130604 (2014).
11. Kjaerby, C., Rasmussen, R., Andersen, M. & Nedergaard, M. Does Global Astrocytic Calcium Signaling Participate in Awake Brain State Transitions and Neuronal Circuit Function? *Neurochem. Res.* **42**, 1810–1822 (2017).
12. Papouin, T., Dunphy, J. M., Tolman, M., Dineley, K. T. & Haydon, P. G. Septal Cholinergic Neuromodulation Tunes the Astrocyte-Dependent Gating of Hippocampal NMDA Receptors to Wakefulness. *Neuron* **94**, 840-854.e7 (2017).
13. Huber, D., Veinante, P. & Stoop, R. Vasopressin and oxytocin excite distinct neuronal populations in the central amygdala. *Science* **308**, 245–8 (2005).
14. Viviani, D. *et al.* Oxytocin selectively gates fear responses through distinct outputs from the central amygdala. *Science* **333**, 104–7 (2011).
15. Han, R. T. *et al.* Long-Term Isolation Elicits Depression and Anxiety-Related Behaviors by Reducing Oxytocin-Induced GABAergic Transmission in Central Amygdala. *Front. Mol. Neurosci.* **11**, 246 (2018).
16. Neugebauer, V., Li, W., Bird, G. C. & Han, J. S. The amygdala and persistent pain. *Neuroscientist* **10**, 221–234 (2004).
17. Tye, K. M. *et al.* Amygdala circuitry mediating reversible and bidirectional control of anxiety. *Nature* **471**, 358–62 (2011).
18. Ji, R.-R., Donnelly, C. R. & Nedergaard, M. Astrocytes in chronic pain and itch. *Nat. Rev. Neurosci.* **20**, 667–685 (2019).
19. Poisbeau, P., Grinevich, V. & Charlet, A. Oxytocin Signaling in Pain: Cellular, Circuit, System, and Behavioral Levels. *Curr. Top. Behav. Neurosci.* (2017). doi:10.1007/7854_2017_14
20. Martin-Fernandez, M. *et al.* Synapse-specific astrocyte gating of amygdala-related behavior. *Nat. Neurosci.* **20**, 1540–1548 (2017).
21. Althammer, F. *et al.* Three-dimensional morphometric analysis reveals time-dependent structural changes in microglia and astrocytes in the central amygdala and hypothalamic paraventricular nucleus of heart failure rats. *J. Neuroinflammation* **17**,

221 (2020).
22. Yizhar, O. *et al.* Neocortical excitation/inhibition balance in information processing and social dysfunction. *Nature* **477**, 171–178 (2011).
23. Lee, H. J., Caldwell, H. K., Macbeth, A. H., Tolu, S. G. & Young, W. S. A conditional knockout mouse line of the oxytocin receptor. *Endocrinology* **149**, 3256–3263 (2008).
24. Wallraff, A. *et al.* The impact of astrocytic gap junctional coupling on potassium buffering in the hippocampus. *J. Neurosci.* **26**, 5438–47 (2006).
25. Robin, L. M. *et al.* Astroglial CB1 Receptors Determine Synaptic D-Serine Availability to Enable Recognition Memory. *Neuron* **98**, 935-944.e5 (2018).
26. Corkrum, M., Rothwell, P. E., Thomas, M. J., Kofuji, P. & Araque, A. Opioid-Mediated Astrocyte-Neuron Signaling in the Nucleus Accumbens. *Cells* **8**, 586 (2019).
27. Robin, L. M. *et al.* Astroglial CB1 Receptors Determine Synaptic D-Serine Availability to Enable Recognition Memory. *Neuron* **0**, 1–10 (2018).
28. Decosterd, I. & Woolf, C. J. Spared nerve injury: an animal model of persistent peripheral neuropathic pain. *Pain* **87**, 149–158 (2000).
29. Thompson, J. M. & Neugebauer, V. Amygdala Plasticity and Pain. *Pain Res. Manag.* **2017**, 8296501 (2017).
30. Gravati, M. *et al.* Dual modulation of inward rectifier potassium currents in olfactory neuronal cells by promiscuous G protein coupling of the oxytocin receptor. *J. Neurochem.* **114**, 1424–1435 (2010).
31. Breton, J.-D. *et al.* Oxytocin-induced antinociception in the spinal cord is mediated by a subpopulation of glutamatergic neurons in lamina I-II which amplify GABAergic inhibition. *Mol. Pain* **4**, 19 (2008).
32. Angulo, M. C., Kozlov, A. S., Charpak, S. & Audinat, E. Glutamate released from glial cells synchronizes neuronal activity in the hippocampus. *J. Neurosci.* **24**, 6920–6927 (2004).
33. Fellin, T. *et al.* Neuronal synchrony mediated by astrocytic glutamate through activation of extrasynaptic NMDA receptors. *Neuron* **43**, 729–43 (2004).
34. Corkrum, M. *et al.* Dopamine-Evoked Synaptic Regulation in the Nucleus Accumbens Requires Astrocyte Activity. *Neuron* **105**, 1036-1047.e5 (2020).
35. Ma, Z., Stork, T., Bergles, D. E. & Freeman, M. R. Neuromodulators signal through astrocytes to alter neural circuit activity and behaviour. *Nature* **539**, 428–432 (2016).
36. Pestana, F., Edwards-Faret, G., Belgard, T. G., Martirosyan, A. & Holt, M. G. No longer underappreciated: The emerging concept of astrocyte heterogeneity in neuroscience. *Brain Sci.* **10**, 1–21 (2020).
37. Khakh, B. S. & Deneen, B. The Emerging Nature of Astrocyte Diversity. *Annu. Rev. Neurosci.* **42**, 187–207 (2019).
38. Grinevich, V. & Neumann, I. D. Brain oxytocin: how puzzle stones from animal studies translate into psychiatry. *Mol. Psychiatry* (2020). doi:10.1038/s41380-020-0802-9
39. Quintana, D. S. *et al.* Advances in the field of intranasal oxytocin research: lessons learned and future directions for clinical research. *Mol. Psychiatry* (2020). doi:10.1038/s41380-020-00864-7
40. Neumann, I. D. & Slattery, D. A. Oxytocin in General Anxiety and Social Fear: A Translational Approach. *Biol. Psychiatry* **79**, 213–221 (2016).
41. Takata, N. *et al.* Optogenetic astrocyte activation evokes BOLD fMRI response with oxygen consumption without neuronal activity modulation. *Glia* **66**, (2018).
42. Figley, C. R. & Stroman, P. W. The role(s) of astrocytes and astrocyte activity in neurometabolism, neurovascular coupling, and the production of functional neuroimaging signals. *Eur. J. Neurosci.* **33**, 577–588 (2011).
43. Kastanenka, K. V. *et al.* A roadmap to integrate astrocytes into Systems Neuroscience. *GLIA* (2019). doi:10.1002/glia.23632
44. Poskanzer, K. E. & Yuste, R. Astrocytes regulate cortical state switching in vivo. *Proc. Natl. Acad. Sci. U. S. A.* **2016**, 1–10 (2016).
45. McCormick, D. A., Nestvogel, D. B. & He, B. J. Neuromodulation of Brain State and Behavior. *Annu. Rev. Neurosci.* **43**, 391–415 (2020).

46. Fenoy, A. J., Goetz, L., Chabardès, S. & Xia, Y. Deep brain stimulation: Are astrocytes a key driver behind the scene? *CNS Neurosci. Ther.* **20**, 191–201 (2014).
47. Monai, H. & Hirase, H. Astrocytes as a target of transcranial direct current stimulation (tDCS) to treat depression. *Neurosci. Res.* **126**, 15–21 (2018).
48. Mills, S. E. E., Nicolson, K. P. & Smith, B. H. Chronic pain: a review of its epidemiology and associated factors in population-based studies. *Br. J. Anaesth.* **123**, e273–e283 (2019).
49. Woo, A. K. Depression and Anxiety in Pain. *Rev. pain* **4**, 8–12 (2010).
50. Oliveira, J. F., Sardinha, V. M., Guerra-Gomes, S., Araque, A. & Sousa, N. Do stars govern our actions? Astrocyte involvement in rodent behavior. *Trends Neurosci.* **38**, 535–49 (2015).
51. Rouach, N., Koulakoff, A., Abudara, V., Willecke, K. & Giaume, C. Astroglial metabolic networks sustain hippocampal synaptic transmission. *Science* **322**, 1551–5 (2008).
52. Pannasch, U. *et al.* Astroglial networks scale synaptic activity and plasticity. *Proc. Natl. Acad. Sci. U. S. A.* **108**, 8467–72 (2011).
53. Theis, M. *et al.* Accelerated hippocampal spreading depression and enhanced locomotory activity in mice with astrocyte-directed inactivation of connexin43. *J. Neurosci.* **23**, 766–76 (2003).
54. Teubner, B. *et al.* Connexin30 (Gjb6)-deficiency causes severe hearing impairment and lack of endocochlear potential. *Hum. Mol. Genet.* **12**, 13–21 (2003).
55. Shigetomi, E. *et al.* Imaging calcium microdomains within entire astrocyte territories and endfeet with GCaMPs expressed using adeno-associated viruses. *J. Gen. Physiol.* **141**, 633–647 (2013).
56. Ting, J. T. *et al.* Preparation of Acute Brain Slices Using an Optimized N-Methyl-D-glucamine Protective Recovery Method. *J. Vis. Exp.* 1–13 (2018). doi:10.3791/53825
57. Serrano, A., Haddjeri, N., Lacaille, J., Robitaille, R. & Centre-ville, S. GABAergic Network Activation of Glial Cells Underlies Hippocampal Heterosynaptic Depression. *J. Neurosci.* **26**, 5370–5382 (2006).
58. Jourdain, P. *et al.* Glutamate exocytosis from astrocytes controls synaptic strength. *Nat. Neurosci.* **10**, 331–9 (2007).
59. Ikegaya, Y., Le Bon-Jego, M. & Yuste, R. Large-scale imaging of cortical network activity with calcium indicators. *Neurosci. Res.* **52**, 132–138 (2005).
60. Shigetomi, E., Bowser, D. N., Sofroniew, M. V & Khakh, B. S. Two forms of astrocyte calcium excitability have distinct effects on NMDA receptor-mediated slow inward currents in pyramidal neurons. *J. Neurosci.* **28**, 6659–63 (2008).
61. Anlauf, E. & Derouiche, A. Glutamine synthetase as an astrocytic marker: its cell type and vesicle localization. *Front. Endocrinol. (Lausanne).* **4**, 144 (2013).
62. Luis-Delgado, O. E. *et al.* Calibrated forceps: A sensitive and reliable tool for pain and analgesia studies. *J. Pain* **7**, 32–39 (2006).
63. Walf, A. A. & Frye, C. A. The use of the elevated plus maze as an assay of anxiety-related behavior in rodents. *Nat. Protoc.* **2**, 322–8 (2007).
64. King, T. *et al.* Unmasking the tonic-aversive state in neuropathic pain. *Nat. Neurosci.* **12**, 1364–1366 (2009).
65. Virtanen, P. *et al.* SciPy 1.0: fundamental algorithms for scientific computing in Python. *Nat. Methods* **17**, 261–272 (2020).
66. Zeisel, A. *et al.* Cell types in the mouse cortex and hippocampus revealed by single-cell RNA-seq. *Science (80-.).* **347**, 1138–1142 (2015).
67. Batiuk, M. Y. *et al.* Identification of region-specific astrocyte subtypes at single cell resolution. *Nat Commun* **11**, 1220 (2020).
68. Kofuji, P. & Araque, A. G-Protein-Coupled Receptors in Astrocyte–Neuron Communication. *Neuroscience* (2020). doi:10.1016/j.neuroscience.2020.03.025
69. Octeau, J. C. *et al.* Transient, Consequential Increases in Extracellular Potassium Ions Accompany Channelrhodopsin2 Excitation. *Cell Rep.* **27**, 2249-2261.e7 (2019).
70. Reeves, A. M. B., Shigetomi, E. & Khakh, B. S. Bulk loading of calcium indicator dyes to study astrocyte physiology: Key limitations and improvements using morphological

687 maps. *J. Neurosci.* **31**, 9353–9358 (2011).
688

FIGURE TITLES AND LEGENDS

Figure 1. Specific CeL astrocytes express oxytocin receptors. (**a**) Overview of CeA fluorescent *in situ* hybridization of OTR mRNA (red) and glutamine synthase immunostaining (GS, green). (**b**) High magnification images of cells positive for OTR mRNA and/or GS (double arrows); green arrows point GS positive cells; red arrows point OTR mRNA-positive cells. Scale bars are 100 (a) and 10µm (b). (**c**) Proportion of CeL astrocytes (GS positive cells, left) and neurons (NeuN positive cells, right) positive for OTR mRNA (red) ($n_{astrocytes}$ = 1185, $n_{neurons}$ = 1254, n_{rats} = 4). (**d**) Cells were reconstructed in 3D using Imaris and morphological parameters were evaluated. Scale bar = 20µm (**e**) OTR-expressing astrocytes are bigger and more complex as indicated by several morphological parameters (cell volume, surface, number of processes, process length and domain volume). (**f**) OTR-expressing astrocytes display a more complex morphology as revealed by Sholl analysis. All data are expressed in mean ± SEM except for violin plots where hatched line represent the median and the dot lines are the first and third quartiles. *** $p < 0.0001$, student's *t*-test or two-way ANOVA followed by Tukey post-hoc test. (Statistics in Extended Data Table 1).

Figure 2. Astrocytic OTR activation evokes calcium transients in CeL astrocytes of rats and mice. (**a**) Experimental strategy to express the ChR1/VChR1 chimaera channel rhodopsin variant C1V1 in OTergic neurons (OxytOpto). (**b**) Experimental scheme of the horizontal CeA slice preparation used, showing C1V1 expressing OT axons (yellow) arising from PVN and projecting to the CeL. (**c**) Typical traces of relative changes in intracellular calcium in astrocytes (ΔF) induced by the activation of C1V1 in OT axons located in the CeL through λ542 nm light pulses (10 ms width, 30 Hz, duration 20 s). (**d**) Proportion of responding astrocytes (left), AUC of ΔF traces (middle) and Ca^{2+} transients frequency (right) normalized to baseline values following C1V1 activation in CeL OT axons, n slice (n_s) = 7, n astrocytes (n_a) = 36. (**e**) (left) Images of CeL astrocytes identified through SR101 (red, top) and corresponding pseudo-color images of OGB1 fluorescence during baseline and after drug application (middle, bottom, stacks of 50 images over 25s of recording). Scale bar = 10µm. (right) Typical ΔF traces following TGOT+TTX (Ctrl) application (**f**) Proportion of responding astrocytes (left), AUC of ΔF traces (middle) and Ca^{2+} transients frequency (right) normalized to baseline values following application of TGOT (0.4 µM) with TTX (1 µM) (Ctrl, n_s = 18, n_a = 136), without TTX (No TTX, n_s = 7, n_a = 43), and with an OTR antagonist (dOVT, 1 µM; n_s = 3, n_a = 24). Data are expressed as means across slices plus SEM (**g**) Experimental strategy for the specific deletion of OTRs in mice CeL astrocytes. (**h**) (left) Example pictures of OTR mRNA (red) and GS (green) labelling in mice injected with P_{GFAP}-GFP-IRES-Cre (top) or P_{GFAP}-GFP rAAV vector (bottom) ; (right) Proportion of CeL astrocytes (GS positive cells) also positive for OTR mRNA (left, blue, P_{GFAP}-GFP: $n_{astrocytes}$ = 1340, n_{mice} = 3 ; right, red P_{GFAP}-GFP-IRES-Cre: $n_{astrocytes}$ = 1561, n_{mice} = 4). Scale bar = 50µm. (**i**) Proportion of responding astrocytes (left), AUC of ΔF traces (middle) and Ca^{2+} transients frequency (right) normalized to baseline values following application of TGOT+TTX in control (blue, n_s = 12, n_a = 237) or GFAP OTR KO mice (red, n_s = 5, n_a = 47; red) acute brain slices. Calcium imaging data are expressed as means across slices plus SEM and white circles indicate averages across astrocytes per slices. * $p < 0.05$, ** $p < 0.01$, *** $p<0.001$, Unpaired *t*-test or Mann-Whitney U test. (Statistics in Table Extended Data Table 2).

Figure 3. OTR-expressing CeL astrocytes are positioned to recruit a CeL astrocyte network through gap junction. (**a**) (left) The distance between two OTR+ astrocytes is larger than the distance between two OTR- astrocytes. (right) OTR+ astrocytes predominantly form contacts with OTR- astrocytes, ($n_{astrocytes}$ = 1270, $n_{OTR+\ astrocytes}$ = 236, n_{rats} = 4). Contacts are defined by a proximity of less than 1µm between GFAP-positive fibers/endfeet from two different astrocytes. (**b**) (left) Typical ΔF traces following TGOT+TTX application in presence of CBX (100 µM, top) or PPADS (50 µM, bottom). (right) Proportion of responding astrocytes, AUC of ΔF traces and Ca^{2+} transients frequency normalized to baseline values following application of TGOT+TTX (0.4 µM) in presence of CBX (n_s = 9, n_a = 75) or PPADS (n_s = 7, n_a = 53). (**c**) (left) Typical ΔF traces following TGOT+TTX application in Cx30/Cx43 KO mice brain slices. (right) Proportion of responding astrocytes, AUC of ΔF traces and Ca^{2+} transients frequency normalized to baseline values following TGOT+TTX application in WT mice (n_s = 19, n_a = 78) and in Cx30/Cx43 KO mice acute brain slices (n_s = 17, n_a = 100). Calcium imaging data are expressed as means across slices plus SEM and white circles indicate averages across astrocytes per slices. *p < 0.05, **p < 0.01, ***p < 0.001, unpaired *t*-test or Mann-Whitney U test. (Statistics in Table Extended Data Table 3).

Figure 4. CeL astrocyte activity promotes excitatory transmission into CeL neurons. (**a**) Experimental strategy for the specific expression of C1V1 in mice CeL astrocytes (AstrOpto). (**b**) Experimental scheme of the horizontal CeA slice preparation used, showing a C1V1 expressing astrocytes and a patched CeL neuron, recorded in whole-cell voltage-clamp configuration with bath-applied TTX and bicuculline to isolate mEPSC. (**c**) (left) Proportion of responding astrocytes, AUC of ΔF traces and Ca^{2+} transients frequency following AstrOpto activation (n_s = 12, n_a = 49) (right) Typical ΔF traces following AstrOpto activation. (**d**) Frequency of mEPSCs in CeL neurons before (basal), during (AstrOpto) and after (Wash) AstrOpto activation (λ542 nm, 3 min long, 1 s width pulse at 0,5 Hz; n = 17). (**e**) Example of an astrocyte in CeL patched with a BAPTA-Biocytin filled capillary (white arrow). Biocytin can be seen diffusing in neighboring astrocytes**. f**) Frequency of mEPSCs in CeL neurons before (basal), during (TGOT, 0.4 µM) and after (Wash) TGOT application (left, n=16). This effect can be blocked by loading BAPTA in the CeL astrocyte network (middle, BAPTAstro, n= 11) and by prior incubation of an NMDAR antagonist (right, AP5, 50 µM, n = 9). (**g**) Experimental strategy for the specific deletion of OTRs in mice CeL astrocytes. (**h**) Frequency of mEPSCs in CeL neurons before (basal), during (TGOT, 0.4 µM) and after (Wash) TGOT application in acute brain slice from WT (left, blue, n = 10) and from GFAP OTR KO mice (right, red, n= 8).). Calcium imaging data are expressed as means across slices plus SEM and white circles indicate averages across astrocytes per slices. Patch-clamp data are expressed as averaged frequency plus SEM across cells, linked white circles indicate individual cell values, example traces of the various conditions are displayed on the right. $^{\#}p$ < 0.05, $^{\#\#\#}p$ < 0.001, Friedman and Dunn's Multiple comparisons, *p < 0.05, **p < 0.01, Unpaired *t*-test or Mann-Whitney U test. (Statistics in Table Extended Data Table 4).

Figure 5. CeL astrocyte activity promotes CeL neuron firing. (**a**) Experimental strategy for the specific expression of C1V1 in mice CeL astrocytes (AstrOpto) (**b**) Experimental scheme of the horizontal CeA slice preparation used, showing a C1V1 expressing astrocytes and a patched CeL neuron, recorded in whole-cell current-clamp configuration to record action potentials (APs). (**c**) Frequency of APs in CeL neurons before (basal), during (AstrOpto) and after (Wash) AstrOpto activation (λ542 nm, 3 min long, 1 s width pulse at 0,5 Hz) in control condition (left, n = 10) or following BAPTA loading in the CeL astrocyte network

(right, BAPTAstro, n = 12). (**d**) Frequency of APs in CeL neurons before (basal), during (TGOT, 0.4 µM) and after (Wash) TGOT application (left, n = 9). This effect can be blocked by loading BAPTA in the CeL astrocyte network (middle, BAPTAstro, n = 9) and by prior incubation of the NMDAR antagonist AP5 (right, AP5, 50 µM, n = 7). (**e**) Experimental strategy for the specific deletion of OTRs in mice CeL astrocytes (GFAP OTR KO). (**f**) Frequency of APs in CeL neurons before (basal), during (TGOT, 0.4 µM) and after (Wash) TGOT application in acute brain slices from WT (left, blue, n = 7) and GFAP OTR KO mice (right, red, n = 11). Example traces of the various conditions are displayed on the right. Patch-clamp data are expressed as averaged frequency plus SEM across cells; linked white circles indicate individual cell values. $^{\#}p < 0.05$, $^{\#\#}p < 0.01$, Friedman and Dunn's Multiple comparisons, $^{*}p < 0.05$, $^{***}p < 0.001$, Unpaired *t*-test or Mann-Whitney U test. (Statistics in Table Extended Data Table 5).

Figure 6. Astrocyte-driven CeL neuron activity modifies amygdala output. (**a**) Experimental strategy for the specific expression of C1V1 in mice CeL astrocytes (AstrOpto) (**b**) Experimental scheme of the horizontal CeA slice preparation used, showing a C1V1 expressing astrocytes and a patched CeM neuron, recorded in whole-cell voltage-clamp configuration to record IPSCs. (**c**) Frequency of IPSCs in CeL neurons before (basal), during (AstrOpto) and after (Wash) AstrOpto activation (λ542 nm, 3 min long, 1 s width pulse at 0,5 Hz) in control condition (left, n = 19) or following BAPTA loading in the CeL astrocyte network (right, BAPTAstro, n = 9). (**d**) Frequency of IPSCs in CeL neurons before (basal), during (TGOT, 0.4 µM) and after (Wash) TGOT application (left, n = 17). This effect can be blocked by loading BAPTA in the CeL astrocyte network (middle, BAPTAstro, n = 17) and by prior incubation of the NMDAR antagonist AP5 (right, AP5, 50 µM, n = 5). (**e**) Experimental strategy for the specific deletion of OTRs in mice CeL astrocytes (GFAP OTR KO). (**f**) Frequency of APs in CeL neurons before (basal), during (TGOT, 0.4 µM) and after (Wash) TGOT application in acute brain slices from WT (left, blue, n = 27) and GFAP OTR KO mice (right, red, n = 15). Example traces of the various conditions are displayed on the right. Patch-clamp data are expressed as averaged frequency plus SEM across cells; linked white circles indicate individual cell values. $^{\#}p < 0.05$, $^{\#\#\#}p < 0.001$, Friedman and Dunn's Multiple comparisons, $^{*}p < 0.05$, $^{**}p < 0.01$, $^{***}p < 0.001$, Unpaired *t*-test or Mann-Whitney U test. (Statistics in Table Extended Data Table 6).

Figure 7. CeL astrocytes modulate CeA behavioral correlates of comfort and are required for their OTR-mediated modulation. (**a, e**) Experimental strategy for the specific expression of C1V1 in mice CeL astrocytes (**a,** AstrOpto) or the specific deletion of OTRs in mice CeL astrocytes (**e,** GFAP OTR KO). The treatments applied are color coded as the legend key indicate. Control indicate a vehicle injection. (**b, f**) 4 weeks after the SNI surgery, mechanical pain threshold was assessed on the neuropathic paw before (Ctrl) and at different time points after either TGOT injection or C1V1 activation of CeL astrocytes (gray arrow) for sham (top) and SNI (bottom, gray box) animals (**c, g**) Anxiety levels were assessed through measurements of the time spent in the closed arms of the elevated plus maze after drugs injections or C1V1 light-driven activation of CeL astrocytes for sham (top) and SNI (bottom, gray box). (**d, h**) Conditioned place preference (CPP) was assessed through measurements of the Δ time spent in the paired chamber before and after pairing. Pairing was realized through drugs injections or C1V1 light-evoked activation of CeL astrocytes for sham (top) and SNI (bottom, gray box). Data are expressed as averages across rats or mice plus SEM. n = 4-18 per group (details and statistics in Extended Data

Table 7). $^{\#}P < 0.001$, $^{\#\#}P < 0.01$ Wilcoxon signed rank test; $^{*}P < 0.05$, $^{**}P < 0.01$, $^{***}P < 0.001$; ANOVA or mixed-design ANOVA followed by posthoc Bonferroni test (Statistics in Table S7). (**i**) Oxytocin-dependent cellular interactions in the CeA. We hypothesize that OT released from axons of PVN neurons within the CeL activates OTR+ astrocytes (red) which consequently spread their activation to neighboring OTR- astrocytes (green) through, at least partly, gap junctions. Subsequently, the CeL astrocytes release D-serine which gates the activation of NMDAR on CeL interneurons, ultimately increasing their firing rate. This in turn inhibits CeM output projection neurons, resulting in anxiolysis and the promotion of a positive emotional state.

METHODS

Animals

Animals were housed under standard conditions with food and water available *ad libitum* and maintained on a 12-hour light/dark cycle and all experiments were conducted in accordance with EU rules and approbation from French Ministry of Research (01597.05). For *ex vivo* and *in vivo* experiments, Wistar rats or C5BL/6 mice were used. *Ex vivo* experiments used animals between 18 and 25 days old, except in experiments where rAAVs were injected, in which case animals were between 2 and 6 months old at the time of sacrifice. *In vivo* experiments used 2-month-old animals at the time of the first surgery.

Specific deletion of OTRs in CeL astrocytes. To specifically ablate OTRs in CeA astrocytes, transgenic cKO mice, in which *loxP* sites flank the OTR coding sequence[23], received bilateral injections (280 nl) of rAAV-GFAP-GFP-IRES-Cre. Following four weeks of expression of the viral proteins, mice were intracardially perfused with 1x PBS and 4% PFA. Brain sections were used for FISH (OTR mRNA) and IHC (GS) to verify the validity of the approach. Representative images and quantifications are provided in Figure 2H, Extended Data Fig. 2g-h.

Specific deletion of Cx30 and Cx43 in astrocytes. To specifically impaire gap-junctions coupling, we used Cx30-/-Cx43fl/fl:hGFAP-Cre mice (Cx30/Cx43 double KO), which were previously characterized[24,51,52], with conditional deletion of Cx43 in astrocytes[53] and additional deletion of Cx30[54].

Cloning and Production of rAAV Vectors:

The generation of rAAVs allowing for the specific expression of the protein of interest in OT-cells is described in our previous work[4]. Briefly, the conserved promoter region of 2.6 kb was chosen using the software BLAT from UCSC (http://genome.ucsc.edu/cgi-bin/hgBlat), was amplified from BAC clone RP24-388N9 (RPCI-24 Mouse, BACPAC Resources, CHORI, California, USA) and was subcloned into a rAAV2 backbone carrying an Ampicillin-resistance.

To construct the OTp-C1V1(t/t)-TS-mCherry AAV vector we used previously cloned OTp-DIO-GFP-WRE plasmid[2] equipped with the characterized 2.6 kb OT promoter[4]. In this plasmid the DIO-GFP sequence was replaced by C1V1(t/t)-TS-mCherry from the rAAV CaMKIIa-C1V1(t/t)-TS-mCherry (Addgene, plasmid #35500).

To generate GFAP-C1V1(t/t)-TS-mCherry AAV vector, we replaced the CamKIIa promoter from the rAAV CaMKIIa-C1V1(t/t)-TS-mCherry by the Gfa promoter from the pZac2.1 gfaABC1D-tdTomato (Addgene, plasmid: 44332). The cell type specificity of the rAAV carrying the Gfa promoter was confirmed[55]. In analogy, the generation of the GFAP-GFP-IRES-Cre vector was achieved using pZac2.1 gfaABC1D-tdTomato (Addgene, plasmid: 44332). First, the promoter was cloned into a rAAV2 backbone and sticky ends were blunted with EcoR1 and Basrg1. Next, pAAV-CamKIIa-C1V1(t/t)-TS-mCherry was blunted using BamHI and BsrGI. Finally, the pBS-ires cre construct was used and IRES-Cre was inserted into the GFAP-driven vector resulting in the GFAP-GFP-IRES-Cre construct.

Production of chimeric virions (recombinant Adeno-associated virus 1/2; rAAV 1/2) was described in[4]. Briefly, human embryonic kidney cells 293 (HEK293; Agilent #240073) were calcium phosphate-transfected with the recombinant AAV2 plasmid and a 3-helper system. rAAV genomic titers were determined with QuickTiter AAV Quantitation Kit (Cell Biolabs, Inc., San Diego, California, USA) and are ~10^{13} genomic copies per ml for all rAAV vectors used in this study.

Surgeries

Neuropathic Pain Model: Spared Nerve Injury (SNI) Procedure

Animals were randomly separated in two groups to undergo either posterior left hindpaw SNI or sham procedure, with right hindpaw untouched. Animals were anaesthetized using isoflurane at 1.5–2.5%. Incision was made at mid-thigh level using the femur as a landmark and a section was made through the biceps femoris. The three peripheral branches (sural, common peroneal and tibial nerves) of the sciatic nerve were exposed. Both tibial and common peroneal nerves were ligated using a 5.0 silk suture and transected. The sural nerve was carefully preserved by avoiding any nerve stretch or nerve contact[28]. For animals undergoing sham surgery, same procedure was performed but nerves remained untouched. Animals were routinely observed daily for 7 days after surgery and daily tested by the experimenter (Extended Data Fig. 6). Besides observing weight, social and individual behavior, the operated hindpaw was examined for signs of injury or autotomy. In case of autotomy or suffering, the animal was euthanized in respect of the ethical recommendations of the EU. No analgesia was provided after the surgery in order to avoid interference with chronic pain mechanisms and this is in accordance with our veterinary authorization. Suffering was minimized by careful handling and increased bedding.

Stereotaxic Surgery: Injections of rAAV Vectors

Stereotaxic surgery was performed under deep ketamine-xylazine anesthesia, using the KOPF (model 955) stereotaxic system. For specific control of rats CeA astroglial cells, 200 nl of rAAV serotype 1/2 (GFAPp-C1V1(t/t)-mCherry, cloned from plasmids #35500 and 44332, Addgene) were injected bilaterally at the coordinates corresponding to CeL: rostro-caudal: -2.7mm, medio-lateral: 4.2mm, dorso-ventral: -8.0mm (From Paxinos and Watson Atlas). For specific control of OT neurons, 200 nl of rAAV serotype 1/2 (OTp-C1V1(t/t)-mCherry or OTp-ChR2-mCherry) were injected bilaterally at the coordinates corresponding to each hypothalamic OT nuclei. PVN: rostro-caudal: -1.8mm; medio-lateral: +/-0.4mm; dorso-ventral: -8.0mm; SON: rostro-caudal: -1.4mm; medio-lateral: +/-1.6mm; dorso-ventral: -9.0mm; AN: rostro-caudal: -2mm; medio-lateral: +/-1.2mm; dorso-ventral: -8.5mm (From Paxinos and Watson Atlas). For specific deletion of OTR in mice CeL astrocytes, 280 nl of rAAV serotype 1/2 (GFAPp-GFP-IRES-Cre) were injected bilaterally at the coordinates corresponding to CeL: rostro-caudal: -1.4mm, medio-lateral: +/-2.6mm, dorso-ventral: -4.3mm (From Paxinos and Watson Atlas) in OTR cKO mice.

Stereotaxic Surgery: intra-CeL Cannulae

Cannulae Implantation. Animals were bilaterally implanted with guide cannulae for direct intra-CeL infusions. As guide cannulae we used C313G/Spc guide metallic cannulae (Plastics one, VA, USA) cut 5.8 mm below the pedestal. For this purpose, animals were deeply anesthetized with 4% isoflurane and their heads were fixed in a stereotaxic frame. The skull was exposed and two holes were drilled according to coordinates that were adapted from brain atlas (rat, 2.3 mm rostro-caudal; 4 mm lateral; 7.5 mm dorso-ventral relative to bregma; mice, 1.4 mm rostro-caudal; 2.6 mm lateral; 4.3 mm dorso-ventral relative to bregma) by comparing the typical bregma-lambda distance with the one measured in the experimental animal. Two screws were fixed to the caudal part of the skull in order to have an anchor point for the dental cement. Acrylic dental cement was finally used to fix the cannulae and the skin was sutured. In case of long lasting experiments (neuropathy-induced anxiety) with a cannula implantation at distance of the behavioral assay (> 4 weeks), cannulae were sometimes lost or cloaked, and concerned animals therefore excluded from testing.

Drugs Infusions. We used bilateral injections of 0.5 µl containing either vehicle (NaCl 0.9%) or oxytocin receptor agonist TGOT (1 µM) dissolved in NaCl 0.9%. For this procedure two injectors (cut to fit 5.8 mm guide cannulae protruding 2 to 2.5 mm beyond the lower end of the cannula in older animals and 1.8 mm in 3-4 week old rats) were bilaterally lowered into the guide cannula, connected via polythene tubing to two Hamilton syringes that were placed in an infusion pump and 0.5 µl of liquid was injected in each hemisphere over a 2-minute period. After the injection procedure, the injectors were kept in place for an additional minute in order to allow a complete diffusion of liquid throughout the tissue. Rats were subsequently left in the home cage for 15 minutes to recover from the stress of the injection and then handled for mechanical pain threshold or anxiety assessment. Animals that received TGOT injections for the first experiment (mechanical sensitivity assessment) were switched to the vehicle injected groups for the elevated plus maze experiment.

Stereotaxic Surgery: intra-CeL Optical Fiber

Optical Fiber Implantation. Sham and rAAVs injected animals both underwent a single surgical procedure in which after vector injection or no injection for sham, optical fibers designed to target the CeL were implanted and firmly maintained on the skull using dental cement. See "***cannulae implantation*"** for the surgical procedure. Implantable optical fibers were homemade using optical fiber cut at appropriate length (FT200EMT, Thorlabs, NJ, USA) inserted and glued using epoxy based glue in ferrules (CFLC230-10, Thorlabs, NJ, USA).

Horizontal and Coronal Slices

Slices Preparations. In all cases, animals were anaesthetized using ketamine (Imalgene 90 mg/kg) and xylazine (Rompun, 10 mg/kg) administered intraperitoneally. Intracardiac perfusion was then performed using one of the following artificial cerebrospinal fluids (aCSFs) dissection solutions. For animals between 18 and 25 days old, an ice-cold sucrose based dissection aCSF was used containing (in mM): Sucrose (170), KCl (2.5), NaH_2PO_4 (1.25), $NaHCO_3$ (15), $MgSO_4$ (10), $CaCl_2$ (0.5), HEPES (20), D-Glucose (20), L-Ascorbic acid (5), Thiourea (2), Sodium pyruvate (3), N-Acetyl-L-cysteine (5), Kynurenic acid (2). For animals between 2 and 6 months old, an ice-cold NMDG based aCSF was used containing

(in mM): NMDG (93), KCl (2.5), NaH_2PO_4 (1.25), $NaHCO_3$ (30), $MgSO_4$ (10), $CaCl_2$ (0.5), HEPES (20), D-Glucose (25), L-Ascorbic acid (5), Thiourea (2), Sodium pyruvate (3), N-Acetyl-L-cysteine (10), Kynurenic acid (2). In both cases, pH was adjusted to 7.4 using either NaOH or HCl, this after bubbling in 95% O_2-5% CO_2 gas, bubbling which was maintained throughout the duration of use of the various aCSFs. Those aCSFs formulae were based on the work of[56]. Following decapitation, brain was swiftly removed in the same ice-cold dissection aCSFs as for intracardiac perfusion, and 350 µm thick horizontal slices containing the CeA was obtained using a Leica VT1000s vibratome. For experiments in Extended Data Fig. 2a-b, coronal slices of the same thickness containing the PVN were used. Upon slicing, brain slices were hemisected and placed, for 1 hour minimum before any experiments were conducted, in a room tempered holding chamber, containing normal aCSFs. For 2 to 6 month old animals, slices were first let for 10 minutes in 35°C NMDG aCSF before placing them in the holding chamber at room temperature. Normal aCSF, also used during all *ex vivo* experiments, is composed of (in mM): NaCl (124), KCl (2.5), NaH_2PO_4 (1.25), $NaHCO_3$ (26), $MgSO_4$ (2), $CaCl_2$ (2), D-Glucose (15), adjusted for pH values of 7.4 with HCL or NaOH and continuously bubbled in 95% O_2-5% CO_2 gas. All aCSFs were checked for osmolality and kept for values between 305-310 mOsm/L. In electrophysiology or calcium imaging experiments, slices were transferred from the holding chamber to an immersion recording chamber and superfused at a rate of 2 ml/min with normal aCSFs unless indicated otherwise.

Drug Application. OTR agonists were bath applied through a 20s long pumping of agonist solution, corresponding to several times the volume of the recording chamber. Other drugs (antagonists, TTX, *etc.*) were applied for at least 20 minutes in the bath before performing any experiments. BAPTA (or BAPTA-free solution for controls) loading of CeL astrocytes was realized following[57] protocol. Two distant CeL astrocytes per slice (label with SR101, 1 µM) were patched in whole cell configuration and voltage steps were applied (2 Hz, ∆40 mV) to help loading the BAPTA contained in the patch pipette (in mM): $MgCl_2$ (1), NaCl (8), $ATPNa_2$ (2) $GTPNa_2$ (0.4) HEPES (10), BAPTA (40) and osmolality checked to be between 275-285 mOsm/l. The whole cell configuration was maintained during 45 min to allow BAPTA diffusion into the astrocyte network[58].

Calcium Imaging and Identification of Astrocytes

To identify astrocytes, SR101 (1 µM) was added to aCSF in a culture well and slices were incubated for 20 minutes at 35°C. The specificity of SR101 labelling to astrocytes of the CeL was verified through patch-clamp experiments, the results of which can be found in Extended Data Fig. 2c-d. The synthetics calcium indicators OGB1 or Rhod-2 was bulk loaded following an adapted version of the method described previously[59] reaching final concentrations of 0.0025 % (~20 µM) for calcium indicators, 0.002% Cremophor EL, 0.01 % Pluronic F- 127 and 0.5% DMSO in aCSF, and incubated for 45 to 60 minutes at 38°C. Upon incubation time, slices were washed in aCSF for at least an hour before any recording was performed. Astrocytes recorded for this study were those co-labeled, in rats for SR101 and OGB1 and in mice for GFP and Rhod2. The spinning disk confocal microscope used to perform astrocyte calcium imaging was composed of a Zeiss Axio examiner microscope with a 40x water immersion objective (numerical aperture of 1.0), mounted with a X-Light Confocal unit – CRESTOPT spinning disk. Images were acquired at 2Hz with either a Rolera em-c² emCCD or an optiMOS sCMOS camera (Qimaging, BC, Canada). Cells within a confocal plane were illuminated for 100 to 150 ms for each wavelength (SR101 and Rhod-2: 575 nm, OGB1 and GFP: 475 nm) using a Spectra 7 LUMENCOR. The different hardware elements were

synchronized through the MetaFluor software (Molecular Devices, LLC, Ca, USA) which was also used for online. Astrocytic calcium levels were measured in hand drawn ROIs comprising the cell body plus, when visible, proximal processes. In all recordings, the Fiji rolling ball algorithm was used to increase signal/noise ratio. Further offline data analysis was performed using a custom written python-based script available on editorial website. Intracellular calcium variation was estimated as changes in fluorescence signals. To take into account micro-movements of the specimen on long duration recordings, the fluorescence values were also calculated for SR101 (or GFP) and subsequently subtracted to the ones of OGB1 (or Rhod2), except in the case of Figure 2a-d, where astrocytes were identified through SR101 fluorescence after the recordings, to avoid unwanted stimulation of the C1V1 opsin. On this last case, recordings in which movements / drifts were visible were discarded. Then, a linear regression and a median filter was applied to each trace. Calcium transients was detected using the find_peaks function of the SciPy library. More precisely, fluorescence variation was identified as a calcium peak if its prominence exceeds the standard deviation (or two times the standard deviation for recordings acquired with the sCMOS camera) and if the maximum peak value surpasses 50 fluorescence units (or 3 units for sCMOS recordings). ROI with zero calcium variations were excluded from the analysis. The remaining ROI were considered as living astrocytes and the number of peaks was quantified before and after the drug application. All data were normalized according to the duration of the recording and astrocytes was labelled as “responsive” when their AUC or their calcium transient frequency was increased by at least 20% after drug application. Because the time post-stimulation is longer than the baseline (10 min vs 5 min), the probability of observing a spontaneous calcium peak is stronger post-stimulation. To avoid this bias, astrocytes with only one calcium peak during the whole recording were not considered as responsive. Finally, all data were averaged across astrocytes per slice, and this results was used as statistical unit. All data were expressed as ratio (baseline/drug effect), a ratio of 1 meaning neither an increase nor a decrease of the measured parameter. For inter-ratio comparison, parametric or non-parametric (depending on data distribution) unpaired statistical tests were used. Fiji software was also used on SR101 / OGB1 pictures to produce illustrative pictures. All calcium imaging experiments was conducted at controlled room temperature (26°C).

Electrophysiology

Whole cell patch-clamp recordings of CeL neurons, CeL astrocytes and CeM neurons were visually guided by infrared oblique light visualization of neurons and completed by SR101 fluorescence observation for astrocytes. Patch-clamp recordings were obtained with an Axon MultiClamp 700B amplifier coupled to a Digidata 1440A Digitizer (Molecular Devices, CA, USA). Borosilicate glass electrodes (R = 3.5 - 7 MΩ) with inner filament (OD 1.5 mm, ID 0.86 mm; Sutter Instrument, CA USA) were pulled using a horizontal flaming/brown micropipette puller (P97; Sutter Instrument, CA, USA). Recordings were filtered at 2 kHz, digitized at 40 kHz and stored with the pClamp 10 software suite (Molecular Devices; CA, USA). Analysis of patch-clamp data were performed using Clampfit 10.7 (Molecular Devices; CA, USA) and Mini analysis 6 software (Synaptosoft, NJ, USA) in a semi-automated fashion (automatic detection of events with chosen parameters followed by a visual validation).

Whole-Cell Recording of CeL Neurons. Recording pipettes were filled with an intracellular solution containing (in mM): $KMeSO_4$ (125), $CaCL_2$ (2), EGTA (1), HEPES (10), $ATPNa_2$ (2), $GTPNa_2$ (0.3). The pH was adjusted to 7.3 with KOH and osmolality checked to be between

290-295 mOsm/l, adjusted with sucrose if needed. For miniature excitatory post synaptic currents (mEPSCs) recordings, neurons were recorded in voltage clamp and hold at a membrane potential of -65 mV. For action potentials (APs) recordings, neurons were recorded in current clamp and hold at I = 0. Series capacitances and resistances were compensated electronically throughout the experiments using the main amplifier. For mEPSCs measurements in CeL neurons (Figure 4), whole cell recordings were conducted in a Mg^{2+} free aCSF, also containing biccuculin (10 µM) and TTX (1 µM) as in[60]. Average events frequencies per cell were calculated on 20s windows, chosen for TGOT or photostimulation during maximal effect, as determined by the visually identified maximal slope of the cumulative plot of the number of events. CeM neurons were classified as TGOT-responsive when the average event frequency was increased by at least 20% during 20s after TGOT application when compared to baseline average frequency. Baseline and recovery frequencies were measured respectively at the beginning and end of each recording. All patch-clamp experiments were conducted at room temperature.

Biocytin Filling of CeL Astrocytes. In the lateral part of the central amygdala slices visualized with infrared-differential contrast optics, astrocytes were identified by their morphological appearance revealed by SR101 and the absence of action potentials in response to depolarizing current injections. Cells were patched with pipettes filled with (in mM) 110 K-Gluconate, 30 KCl, 4 $ATPNa_2$, 10 phosphocreatine, 0.3 $GTPNa_2$, 10 HEPES and 5 biocytin (pH: 7.3; 310 mOsm). After obtaining whole-cell configuration astrocytes were hold at -80 mV and typical filling time was 45 minutes. Then the pipettes were carefully retracted and slices were incubated for additional 20 minutes in the oxygenated aCSF before fixation. Only one cell was filled per slice. Slices with filled cells were immersion-fixed at 4°C for 5 days in 4% PFA-PBS solution. Next, the slices were flat-embedded in 6% Agar-PBS, areas of interest were cut out of, re-embedded onto the Agar block and Vibratome-cut into 80 µm thick free-floating sections. The sections then were incubated with Avidin conjugated to Alexa Fluor488 (1:1000) (Thermo Fisher) in 1% Triton-PBS at 4°C, washed in PBS, mounted and cover-slipped. The tissue was analyzed and images taken at Leica TCS SP5 Confocal Microscope.

Whole-cell Recording of CeM Neurons. Pipettes were filled with an intracellular solution containing (in mM): KCl (150), HEPES (10), $MgCl_2$ (4), $CaCl_2$ (0.1), BAPTA (0.1), $ATPNa_2$ (2), $GTPNa_2$ (0.3). pH was adjusted to 7.3 with KOH and osmolality checked to be between 290-295 mOsm/L, adjusted with sucrose if needed. All cells were hold at a membrane potential of -70 mV. Series capacitances and resistances were compensated electronically throughout the experiments using the main amplifier. Average events frequencies per cell were calculated on 20s windows, chosen for TGOT or photostimulation during maximal effect, as determined by the visually identified maximal slope of the cumulative plot of the number of events. CeM neurons were classified as TGOT-responsive when the average IPSCs frequency was increased by at least 20% during 20s after TGOT application when compared to baseline average frequency. Baseline and recovery frequencies were measured respectively at the beginning and end of each recording. All patch-clamp experiments were conducted at room temperature.

Immunohistochemistry and *in situ* Hybridization

In situ *Hybridization for OTR mRNA in Rat CeL.* The probe for OTR mRNA was *in vitro* transcripted from a 902-bp fragment containing 133-1034 bases of the rat OTR cDNA (NCBI Reference Sequence: NM_012871.3) subcloned into pSP73 Vector (Promega). The digoxigenin (DIG)-labeled antisense and sense RNA probe from the linearized *oxtr* cDNA template was synthesized using DIG RNA Labeling Kit (SP6/T7) (Roche Diagnostics). Sections containing 2 consecutive sections of the CeL (corresponding to Bregma: 2.5) were processed for fluorescent *in situ* hybridization (FISH). Rats were transcardially perfused with PBS followed by 4% PFA. Brains were dissected out and post fixed overnight in 4% PFA at 4°C with gentle agitation. 50 µm vibratome sections were cut, collected and fixed in 4% PFA at 4°C overnight. The free-floating sections were washed in RNase-free PBS, immersed in 0.75% glycine in PBS, treated with 0.5 µg/ml proteinase K for 30 min at 37 °C, acetylated with 0.25% acetic anhydride in 0.1 M triethanolamine, and then hybridized with DIG-labeled RNA probe overnight at 65 °C. After RNase treatment and following intensive wash, the hybridized DIG-labeled probe was detected by incubation with Anti-Digoxigenin-POD (1:200; 11207733910; Roche Diagnostics) for 3 days at 4 °C. Signals were developed with tyramid signal amplification method. Rhodamine-conjugated tyramide was synthesized by coupling NHS-Rhodamine (Pierce Biotechnology, Thermo Fisher Scientific) to Tyramine-HCl (Sigma-Aldrich) in dimethylformamide with triethylamine. For the quantification of OTR mRNA-positive astrocytes, all confocal images were obtained using the same laser intensities and processed with the same brightness / contrast settings in Adobe Photoshop. Since the *in situ* signal for the OTR mRNA in astrocytes was weak, we first calculated the average intensity (signal intensity of all pixels divided by the total number of pixels) of the rhodamine-stained OTR mRNA signal for each individual section containing the CeL. Next, we calculated the standard deviation for each individual confocal image based on the intensity of all pixels comprising the image. We defined the threshold for OTR mRNA-positive astrocytes: If more than 1/4 of all pixels comprising an astrocyte soma displayed a signal intensity exceeding the average background intensity by more than 4-times the standard deviation, the astrocytes were considered as OTR mRNA-positive.

Astrocytes Markers. The aldehyde dehydrogenase 1 antibody is a commonly used marker for glial cells, including astrocytes. Therefore, we used the ALDH1L1 for immunohistochemistry in our initial experimental studies (Extended Data Fig. 1c, S4a). However, due to inconsistencies in staining quality as a result of batch-dependent antibody properties, especially in combination with the OTR mRNA FISH, we decided to employ Glutamine Synthetase (GS, Figure 1). GS is a commonly used glial marker[61], which stains astrocyte cell bodies, faint processes and even astrocytes not expressing GFAP. Using GS, we achieved consistent results in combination with our OTR mRNA FISH.

Glutamine Synthase, ALDH1L1 Colocalization with OTR mRNA in Rat CeL. After development and washing steps the sections were stained with antibodies against GS (mouse monoclonal, 1:500, ref: MAB302, MerckMilipore), ALDH1L1 (rabbit polyclonal, 1:500, ref: ab87117, abcam), in PBS and kept at 4°C on a shaker in a dark room overnight. After intensive washing with PBS, sections were stained with the respective secondary antibodies AlexaFluor488 (goat anti-mouse, 1:1000, ref: A11001, life technologies) and AlexaFluor680 (goat anti-mouse, 1:1000, ref: A27042, ThermoFischer Scientific) for 2 hours at RT. Following intensive washing with PBS, sections were mounted using Mowiol.

Double* in situ *Hybridizations for OTR mRNA and GFAP mRNA in Mice CeL. Fluorescent *in situ* hybridization (FISH) in Extended Data Fig. 1d was performed on 25-µm cryostat-cut coronal sections prepared from fresh-frozen mouse brain (male C57BL/6J, P22). After extraction, brains were immediately frozen in Tissue-Tek O.C.T. compound and stored at -80 degrees Celsius. ISH was performed according to the manufacturer's instructions (Advanced Cell Diagnostics) for Fresh Frozen RNAscope Multiplex Fluorescent Assay. Treatment of amygdala containing sections were adjusted with the 3-plex negative control and then coexpression of OTR and GS examined using ACD designed target probes as well as the nuclear stain DAPI. Single plan images were collected with an upright laser scanning microscope (LSM-710, Carl Zeiss) using a 40x-objective with keeping acquisition parameters constant between control and probe treated sections.

AAV-GFAP-C1V1(t/t)-mCherry Specificity. After 3 weeks of vector expression in the brain, rats were transcardially perfused with 4% paraformaldehyde solution. Tissue blocks, containing CeA were dissected from the fixed brain and Vibratome-cut into 50 µm thick free-floating sections. After several rinse steps sampled sections were blocked with 5% NGS in PBS and incubated for 48 h at 4°C with polyclonal rabbit anti-ALDH1L1 antibody (1:500, Abcam) in 1% Triton-PBS buffer, containing 0,1 % NGS. Appropriate secondary antibody (AlexaFluor488 conjugated goat anti-rabbit (1:1000, LifeTechnologies) was used for further antigen detection. Intrinsic mCherry fluorescence of vector-expressing cells was strong enough to detect them in the tissue without any additional antibody enhancement. The immunolabeled sections were mounted onto Superfrost slides, cover-slipped with Mowiol, analyzed and documented using LEICA SP5 confocal microscope.

Three-dimensional assessment of astrocyte complexity and interaction analysis using Imaris. For the 3D reconstruction of astrocytes, we took Z-stack images (50 µm depth, 1µm steps, 40x magnification) CeL using a Zeiss LSM 780 confocal microscope (1024x1024 pixel, 16-bit depth, pixel size 0.63-micron, zoom 0.7). Raw czi files were used for further analysis using Imaris software (Version 9.31, Oxford Instruments). First, Imaris was used to reconstruct the astrocyte surface using the following custom settings: surfaces Detail 0.700 µm (smooth); thresholding Background subtraction (Local Contrast), diameter of largest Sphere, which fits into the object: 2.00; Color: base, diffusion transparency: 65%. After surface reconstruction, we used the filter function to remove unspecific background signals: Filter: Volume max – 400 µm 3. It is important to note that these settings have to be adjusted for every new batch / IHC staining to guarantee a reliable reconstruction. All astrocytes with incomplete somata (cut by either the x, y or z plane) were manually removed and not included in further analysis Fused astrocytes that were falsely recognized as one entity by the software were manually separated using the cut function, or entirely removed from the sample if a separation was not feasible. The 'filter/area function' was used to remove small astrocytic segments that occurred during manual deletion. After deletion of all background signals the 'mask all' function was used to create the final surface reconstruction. Next, the surface reconstruction was used as the template for the filament reconstruction using the following custom settings: detect new starting points: largest Diameter 7.00 µm, seed points 0.300 µm; remove seed points around starting points: diameter of sphere regions: 15 µm. Seed points were corrected for (either placed in or removed from the center of the somata) manually if the Imaris algorithm placed them incorrectly. All surface and filament parameters were exported into separate Excel files and used for data analysis. All images used for analysis were taken with the same confocal settings (pinhole, laser intensity, digital gain and

digital offset). Sholl analysis was performed using Imaris in the filament reconstruction mode and individual data sets were exported into separate Excel files for further analysis. each individual sphere) per individual astrocyte. For the nearest neighbor and interaction analysis we used the 'Native Distance Measurements' function as depicted in this video: https://imaris.oxinst.com/learning/view/article/imaris-9-5-native-distance-measurements. In brief, we reconstructed astrocytic surfaces based on the GFAP fluorescence and OTR mRNA signal. Next, we manually labelled OTR+ and OTR- astrocytes and performed the native distance measurement allowing us to assess the shortest distance between GFAP-positive processes of different astrocytes. We defined 'astrocytic interaction' when GFAP-positive processes of two different astrocytes were no further than 1µm apart. It is important to note that this method does not allow the discrimination of different astrocytic entities so that several close contacts (contacts being defined as a distance of less than 1µm between GFAP-positive processes or endfeets from two different astrocytes) originating from the same astrocyte result in a higher number of total interactions. For the nearest neighbor analysis, we calculated the distance from the center of the soma to the nearest astrocyte neighbor using GS fluorescence and an artificially created sphere that was placed within the soma and measured the distance accordingly. Distribution plots and correlations as well as all statistics were performed using GraphPad Prism 8.0.

Optogenetics

Ex vivo. We opted for a ChR1/VChR1 chimaera channel rhodopsin displaying a red-shifted absorption spectrum, referred here as C1V1[22]. This choice was made over a classical channelrhodopsin-2 to avoid unwanted stimulation of OT axons while imaging our 488nm light sensitive calcium indicator (OGB1). Optogenetic green light stimulation of C1V1 in *ex vivo* experiments was performed using either the Spectra 7 LUMENCOR (λ542 nm) or light source X-Cite® 110LED from Excelitas Technologies through a Cy3 filter, controlled via MetaFluor or Clampex driven TTL pulses, respectively.

In vivo. Animals were habituated to the fixation of an optical fiber on the ferrule without light stimulation for one week before the experiment. In all cases, optical fibers were attached to the ferrules using an adapter (ADAF2, Thorlabs, NJ, USA) and animals let free to move in a typical home cage for the duration of the stimulation. Implanted optical fibers were connected to two lasers (LRS-0532-GFM-00100-03 LaserGlow 532nm DPSS Laser System) and the output power adjusted to correspond to 20 to 30 mW measured at the tip of 200 µm diameter fibers similar to the one implanted. Stimulation of 500 ms duration at a frequency of 0.5Hz were given for 3 min.

Behavior

***Mechanical Sensitivity Assessment*.** In experiments with rats, we used a calibrated forceps (Bioseb, Chaville, France) previously developed in our laboratory to test the animal mechanical sensitivity[62]. Briefly, the habituated rat was loosely restrained with a towel masking the eyes in order to limit stress by environmental stimulations. The tips of the forceps were placed at each side of the paw and a graduate force applied. The pressure producing a withdrawal of the paw, or in some rare cases vocalization, was considered as the nociceptive threshold value. This manipulation was performed three times for each hind paw and the values were averaged as being the final nociceptive threshold value. In

experiments with mice, we used von Frey filaments tests. Mechanical allodynia (a symptom of neuropathic pain) was tested using von Frey hairs and results were expressed in grams. Tests were performed during the morning starting at least 2 h after lights on. Mice were placed in clear Plexiglas boxes (7 cm x 9 cm x 7 cm) on an elevated mesh floor. Calibrated von Frey filaments (Bioseb) were applied to the plantar surface of each hindpaw until they just bent in a series of ascending forces up to the mechanical threshold. Filaments were tested five times per paw and the paw withdrawal threshold (PWT) was defined as the lower of two consecutive filaments for which three or more withdrawals out of the five trials were observed.

Elevated Plus Maze. Following protocol from[63], the arena is composed of four arms, two open (without walls) and two closed (with walls; rats 30 cm high; mice 15 cm high). Arms are 10 cm wide, 50 cm long and elevated 50 cm off the ground for rats and 5 cm wide, 30 cm long and elevated 40 cm of the ground for mice. Two lamps with intensity adjustable up to 50 watts were positioned on the top of the maze, uniformly illuminating it. Animals were video tracked using a video-tracking systems (Ethovision Pro 3.16 Noldus, Wageningen, Netherlands and Anymaze, Stoelting Europe, Ireland). After each trial, the maze was cleaned with 70% ethanol and dry with paper towel. Twenty minutes after intracerebral injections or directly after optical stimulation, the animal was let free at the center of the plus maze, facing the open arm opposite to where the experimenter is, and was able to freely explore the entire apparatus for six minutes. Total time and time spend in closed and open arms were recorded in seconds and the percentage of time spent in closed arms was calculated as a measure of anxiety-like behavior. As internal control, the total distance travelled during the test period was quantified and compared between all different groups (Extended Data Fig. 7). Animals falling from the apparatus during the test, freezing more than 50% of the total time, or with cannulae/optic fiber issues, were removed from the analysis.

***Conditioned Place Preference*.** The device is composed of two opaque conditioning boxes (rats: 30x32 cm; mice: 22x22 cm) and one clear neutral box (30x20 cm) Animals were video tracked using a video-tracking system (Anymaze, Stoelting Europe, Irland). After each trial, the device was cleaned with a disinfectant (Surfa'Safe, Anios laboratory). Based on[64], all rats underwent a 3 days habituation period during which they were able to freely explore the entire apparatus for 30 min. On the day 3, behavior was record for 15 min to verify the absence of pre-conditioning chamber preference. The time spend in the different compartment were measured and paired compartment was chosen as the compartment in which rat spent the less time during the 3rd day of habituation. On day 4, animals were placed the morning in one compartment for 15 min with no stimulation (unpaired box). Four hours after, the animal were placed 15 min in the opposite box (paired box) and CeL astrocyte expressing C1V1 vector were optogenetically stimulated (3 min – 1 s light pulse at 0.5 Hz - λ542 nm) or TGOT micro-infused through intracerebral cannulae. On day 5, the animals were place in the CPP box and allowed to freely explore the entire apparatus during 15 min. As internal control, the total distance traveled during the test period was quantified and compared between all different groups (Extended Data Fig. 7). Rats falling spending more than 80% of the total time in a single chamber before the conditioning, or with cannulae/optic fiber issues, were removed from the analysis.

QUANTIFICATION AND STATISTICAL ANALYSIS

All parametrical statistical tests presented in figure captions or manuscript were performed following correct verification of the assumptions on the distribution of data, and if not non-parametric tests were used. Statistical test displayed in the text are not shown on figures. Tests were performed using either GraphPad Prism (version 8.0.0 for Windows, GraphPad Software, San Diego, California USA) or the SciPy Python-based library[65]. All values, group compositions and statistical tests for each experiment and figure panel are detailed in Extended Data Tables 1-7.

SUPPLEMENTARY DISCUSSION – TECHNICAL LIMITATIONS

We acknowledged a number of technical limitations in our study, which are discussed in details here:

mRNA detection. It is surprising to find that the loss of OTR expression in astrocytes results in a loss of function of OTR signaling in the CeA-CeM projection, especially considering the high proportion of OTR+ neurons (up to 70%) compared to the lower fraction of OTR+ astrocytes (18%) in the CeL. One methodological limitation here is that we remained limited to measuring mRNA levels through FISH, and could not measure OTR expression at the protein level, notably due to the poor availability of reliable OTR antibodies. It is also possible that a comparison between the astrocytes' and neurons' contents of OTR mRNA is biased, indeed astrocytes have a lower total mRNA contents than neurons, as publicly available databases of single cell RNA sequencing indicate[66,67]. Interestingly, a similar discrepancy between low receptor levels observed in astrocytes compared to neurons and yet a crucial functional relevance of astrocytes' receptors in neuromodulation is also observed for another GPCR, the CB1 receptor[68] (and references therein).

C1V1 red-shifted opsin to activate astrocytes. It has been recently demonstrated that the activation of such depolarizing channel rhodopsins in astrocytes or neurons can lead to a significant leak of potassium ions in the extracellular space, resulting in increased neuronal excitability[69]. Yet, we provide results in which we buffered the astrocytes intracellular calcium using BAPTA infusion before activating astrocytic C1V1, and found that it abolished its effects on CeA neurons (Fig. 4-6). Furthermore, we demonstrate that the AstrOpto effect on CeA neuronal circuit is dependent on NMDARs (Extended Data Fig. 5a). This indicates that consequences of astrocytic C1V1 activation are dependent on the evoked astrocyte calcium signaling rather than potassium leakage.

Bulk loading of organic calcium indicator dyes. It should also be noted that we used bulk loading of organic calcium indicator dyes. This means we could not precisely measure cytosolic calcium changes in fine astrocyte processes[70], which may have revealed more complex activities of astrocytes. We note it has been proven that endogenous or exogenous (designer receptor exclusively activated by designer drugs receptors, DREADD) GPCR signaling in astrocytes produces a global increase in calcium in both the cell body and processes([68] and references therein).

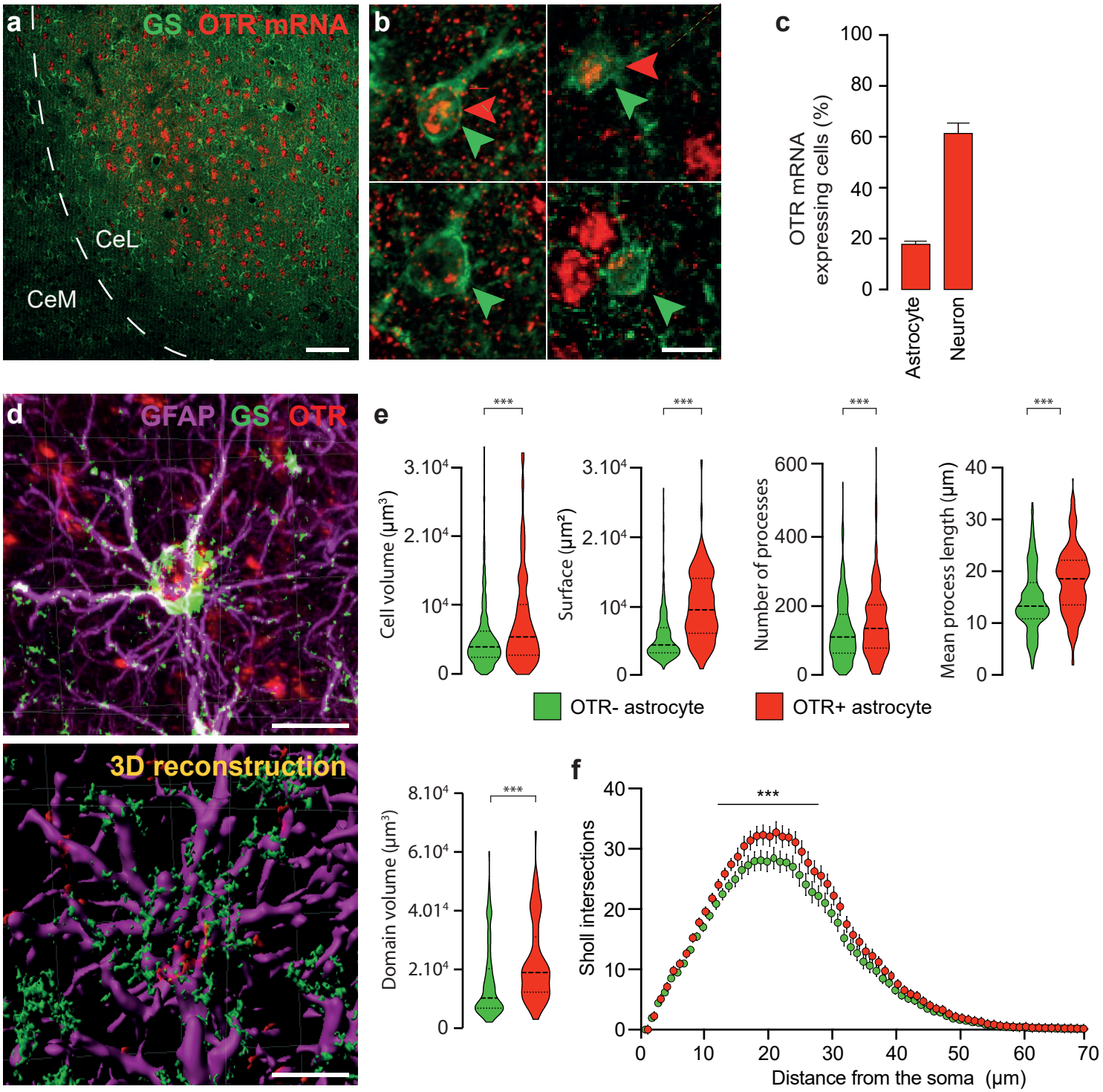
a
GS OTR mRNA
CeL
CeM
b
c
OTR mRNA expressing cells (%)
100
80
60
40
20
0
Astrocyte
Neuron
d
GFAP GS OTR
3D reconstruction
e
***
Cell volume (µm³)
3.10⁴
2.10⁴
10⁴
0
Surface (µm²)
Number of processes
600
400
200
Mean process length (µm)
40
30
20
10
OTR- astrocyte
OTR+ astrocyte
Domain volume (µm³)
8.10⁴
6.10⁴
4.01⁴
2.10⁴
f
Sholl intersections
Distance from the soma (µm)
0
10
20
30
40
50
60
70

Figure 1

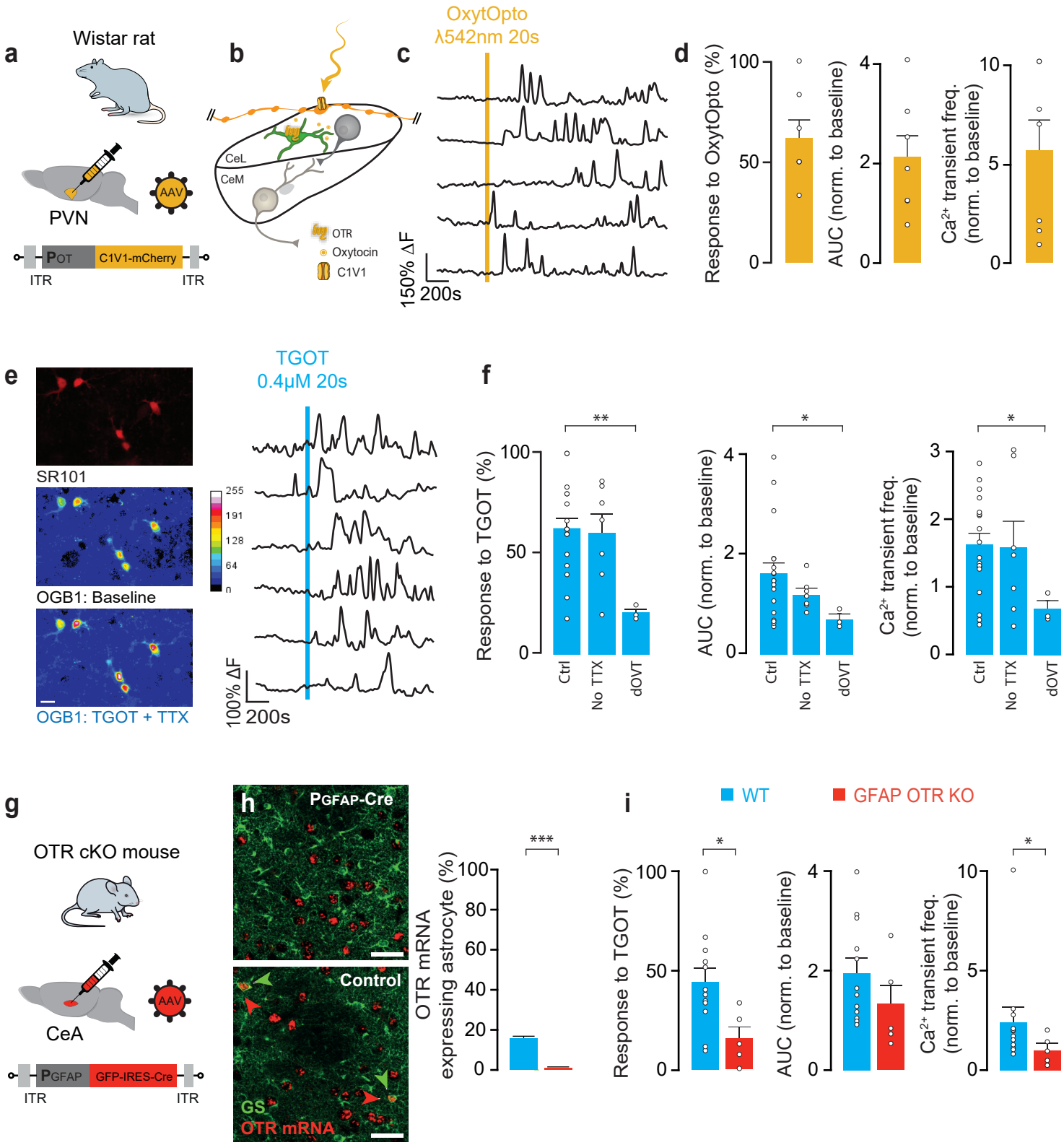
a
Wistar rat
PVN
AAV
POT
C1V1-mCherry
ITR
ITR
b
CeL
CeM
OTR
Oxytocin
C1V1
c
OxytOpto
λ542nm 20s
150% ΔF
200s
d
Response to OxytOpto (%)
AUC (norm. to baseline)
Ca2+ transient freq. (norm. to baseline)
e
SR101
OGB1: Baseline
OGB1: TGOT + TTX
TGOT
0.4μM 20s
255
191
128
64
n
100% ΔF
200s
f
Response to TGOT (%)
AUC (norm. to baseline)
Ca2+ transient freq. (norm. to baseline)
Ctrl
No TTX
dOVT
g
OTR cKO mouse
AAV
CeA
PGFAP
GFP-IRES-Cre
ITR
ITR
h
PGFAP-Cre
Control
GS
OTR mRNA
OTR mRNA expressing astrocyte (%)
i
WT
GFAP OTR KO
Response to TGOT (%)
AUC (norm. to baseline)
Ca2+ transient freq. (norm. to baseline)

Figure 2

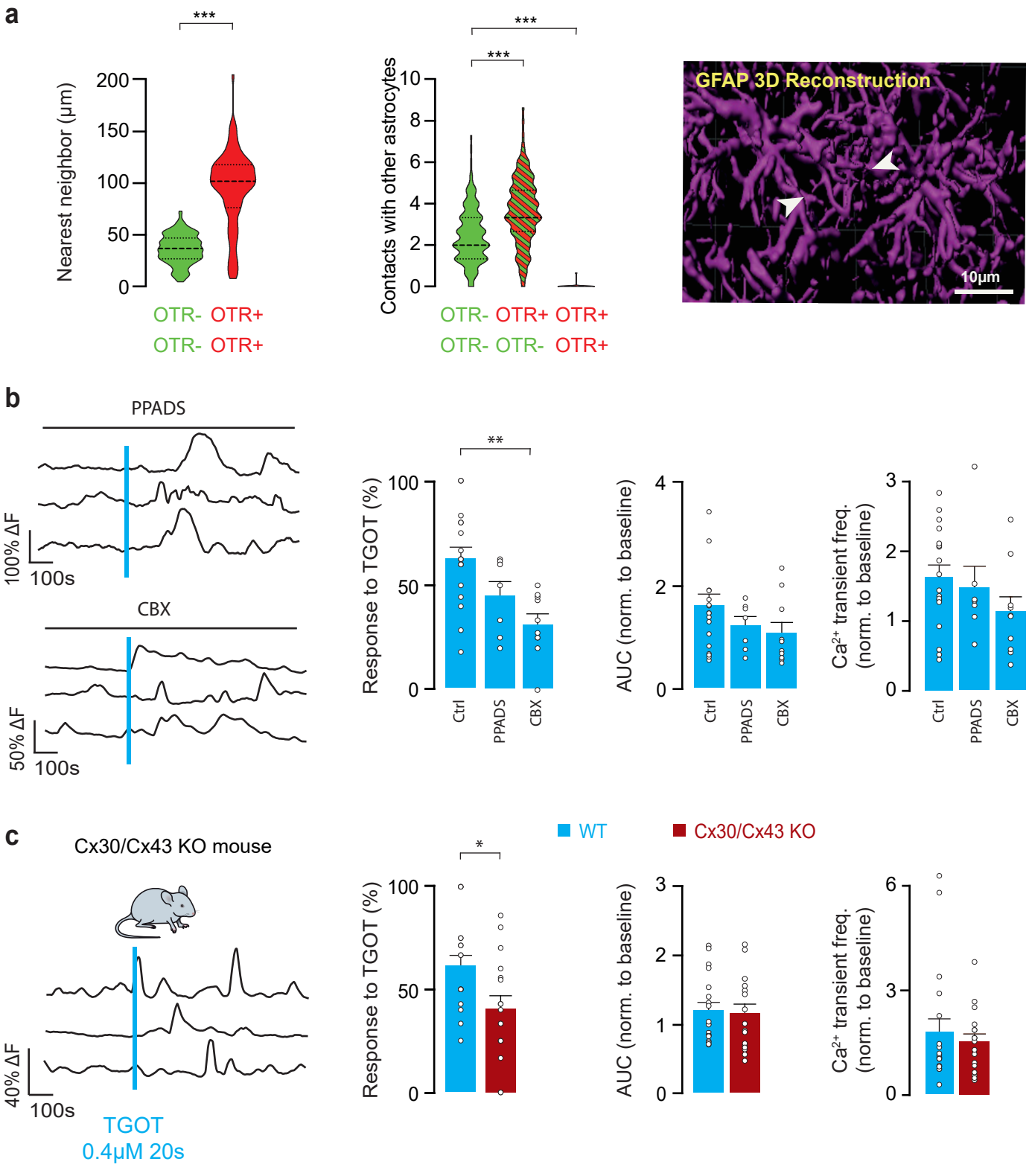
a
***
Nearest neighbor (µm)
200
150
100
50
0
OTR- OTR+
OTR- OTR+
***
***
Contacts with other astrocytes
10
8
6
4
2
0
OTR- OTR+ OTR+
OTR- OTR- OTR+
GFAP 3D Reconstruction
10µm
b
PPADS
100% ΔF
100s
CBX
50% ΔF
100s
**
Response to TGOT (%)
100
50
0
Ctrl
PPADS
CBX
AUC (norm. to baseline)
4
2
0
Ctrl
PPADS
CBX
Ca2+ transient freq. (norm. to baseline)
3
2
1
0
Ctrl
PPADS
CBX
c
Cx30/Cx43 KO mouse
WT
Cx30/Cx43 KO
40% ΔF
100s
TGOT
0.4µM 20s
*
Response to TGOT (%)
100
50
0
AUC (norm. to baseline)
3
2
1
0
Ca2+ transient freq. (norm. to baseline)
6
3
0

Figure 3

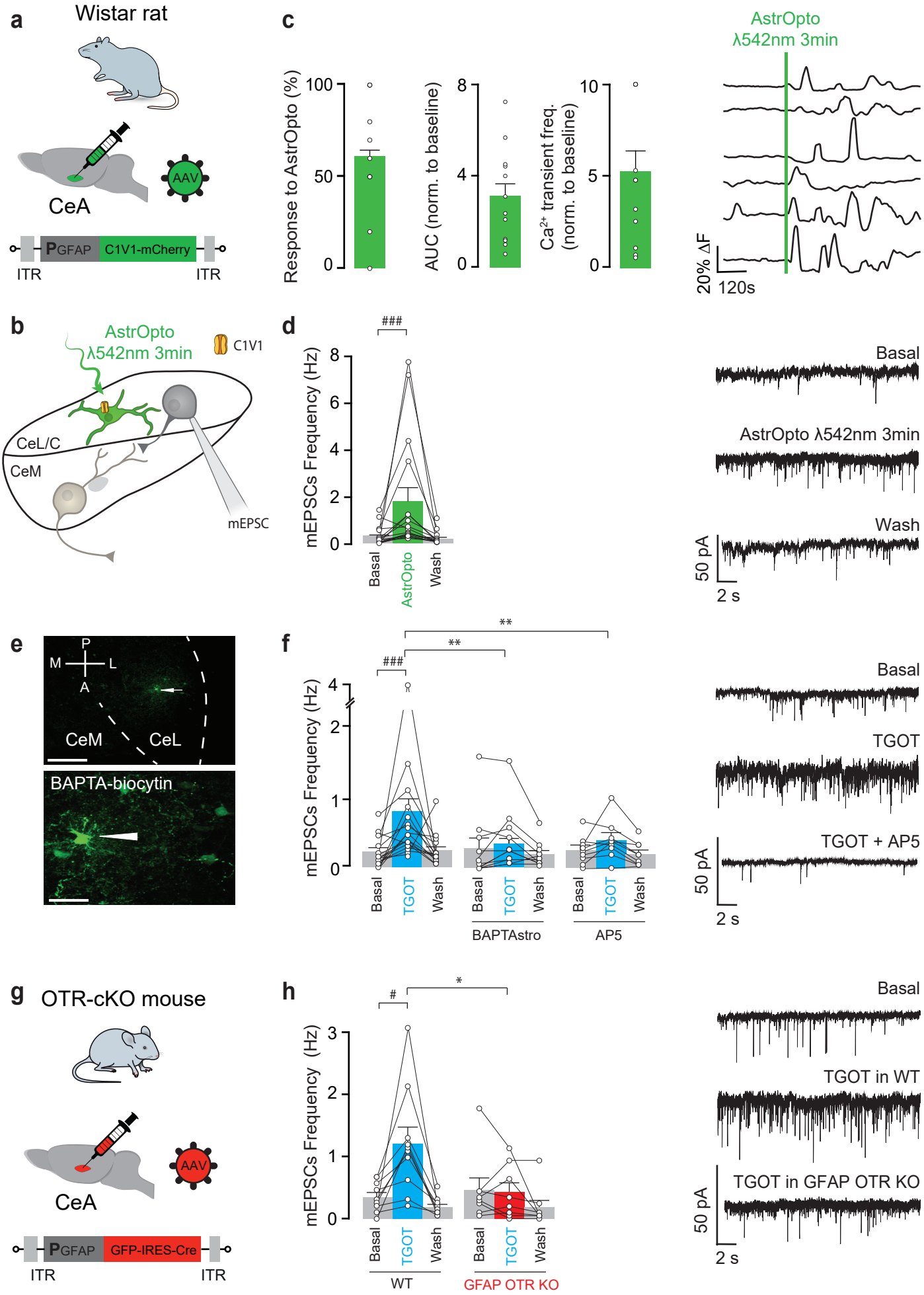
a
Wistar rat
AAV
CeA
PGFAP
C1V1-mCherry
ITR
ITR
b
AstrOpto
λ542nm 3min
C1V1
CeL/C
CeM
mEPSC
c
Response to AstrOpto (%)
100
50
0
AUC (norm. to baseline)
8
4
0
Ca2+ transient freq. (norm. to baseline)
10
5
0
AstrOpto
λ542nm 3min
20% ΔF
120s
d
###
mEPSCs Frequency (Hz)
8
6
4
2
0
Basal
AstrOpto
Wash
Basal
AstrOpto λ542nm 3min
Wash
50 pA
2 s
e
P
M
L
A
CeM
CeL
BAPTA-biocytin
f
**
**
###
mEPSCs Frequency (Hz)
4
2
1
0
Basal
TGOT
Wash
BAPTAstro
AP5
Basal
TGOT
TGOT + AP5
50 pA
2 s
g
OTR-cKO mouse
AAV
CeA
PGFAP
GFP-IRES-Cre
ITR
ITR
h
*
#
mEPSCs Frequency (Hz)
3
2
1
0
Basal
TGOT
Wash
WT
GFAP OTR KO
Basal
TGOT in WT
TGOT in GFAP OTR KO
50 pA
2 s

Figure 4

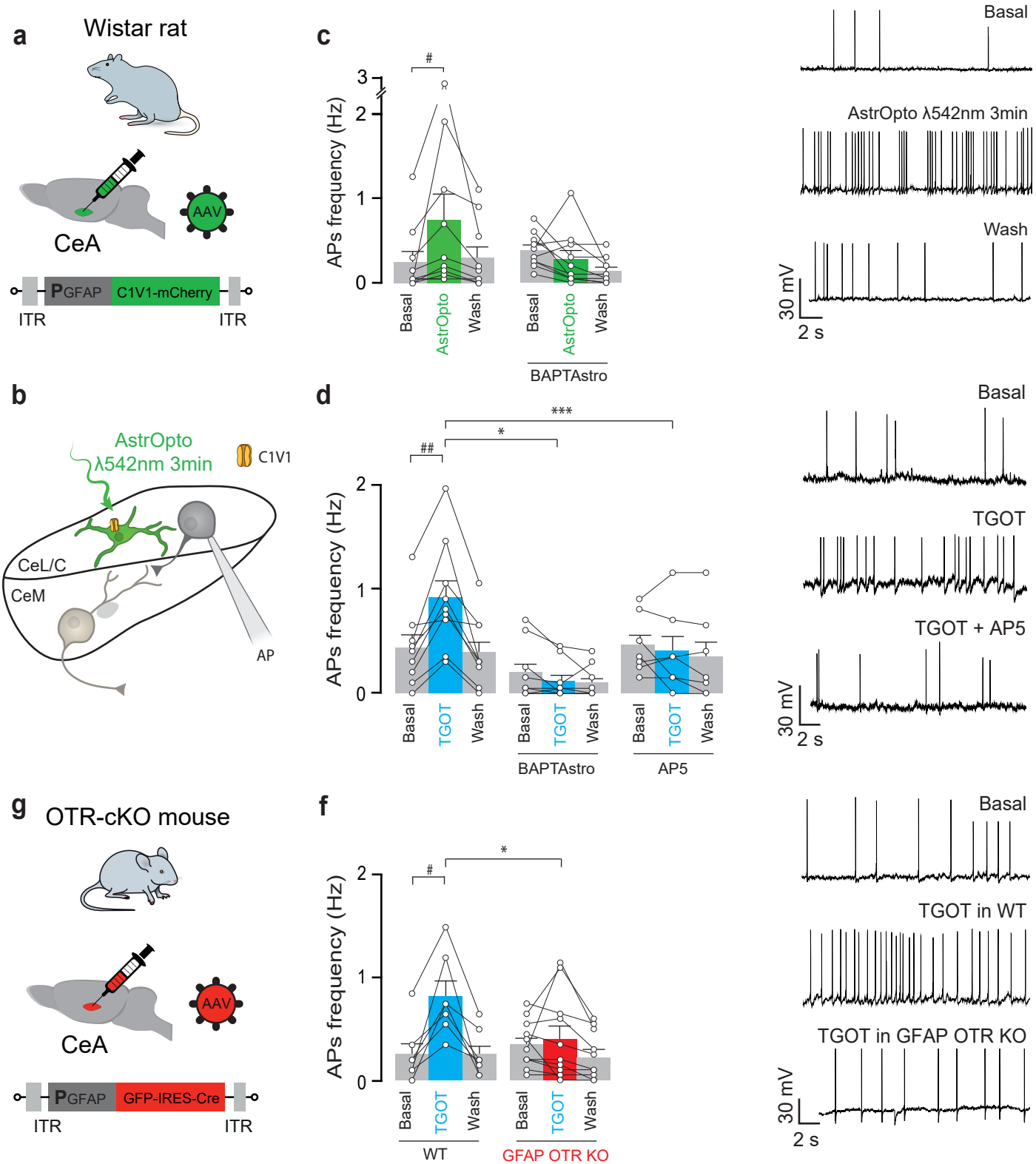
a
Wistar rat
AAV
CeA
PGFAP
C1V1-mCherry
ITR
ITR
b
AstrOpto
λ542nm 3min
C1V1
CeL/C
CeM
AP
c
APs frequency (Hz)
Basal
AstrOpto
Wash
BAPTAstro
Basal
AstrOpto λ542nm 3min
Wash
30 mV
2 s
d
APs frequency (Hz)
Basal
TGOT
Wash
BAPTAstro
AP5
Basal
TGOT
TGOT + AP5
30 mV
2 s
g
OTR-cKO mouse
AAV
CeA
PGFAP
GFP-IRES-Cre
ITR
ITR
f
APs frequency (Hz)
Basal
TGOT
Wash
WT
GFAP OTR KO
Basal
TGOT in WT
TGOT in GFAP OTR KO
30 mV
2 s

Figure 5

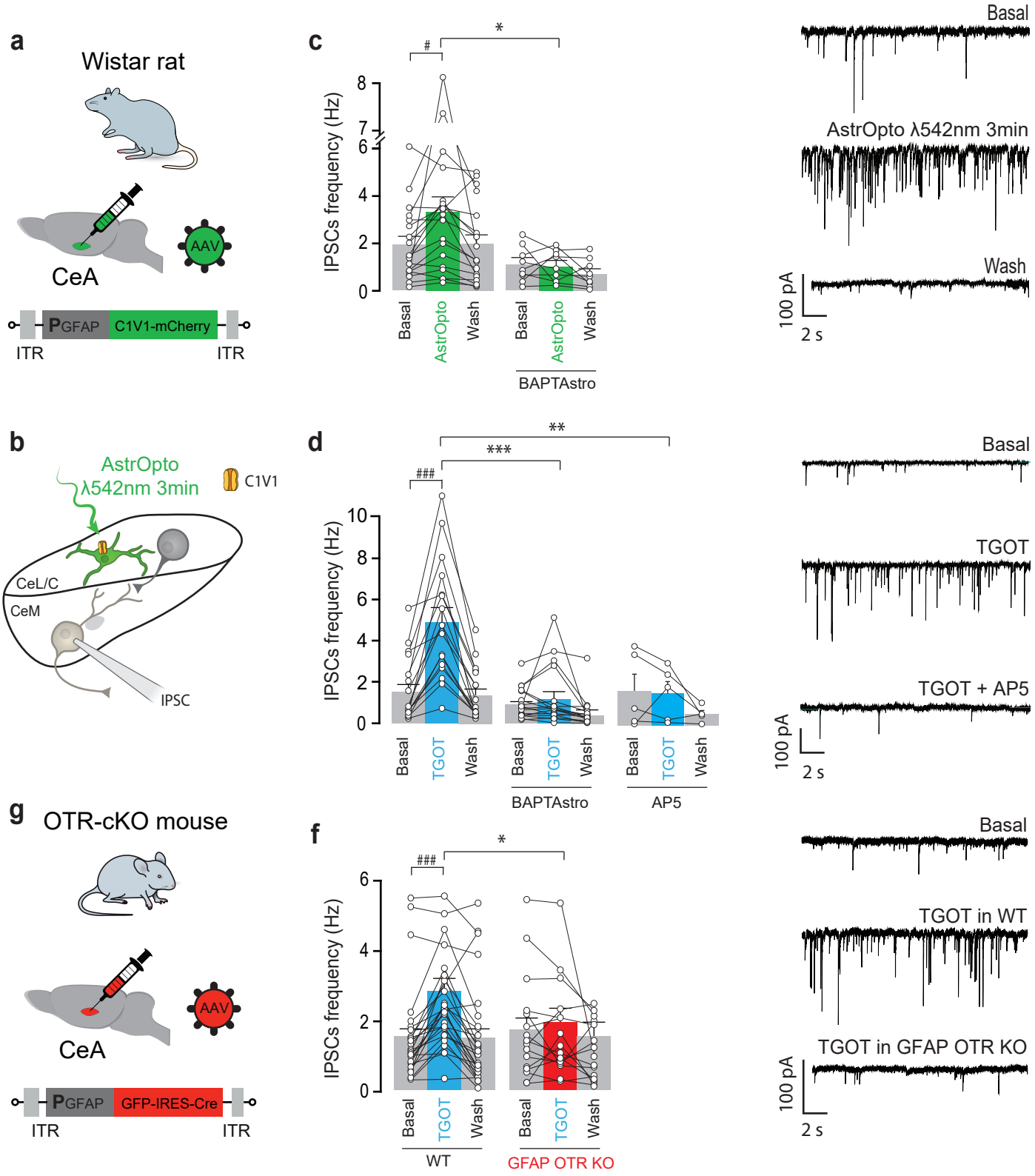
a
Wistar rat
AAV
CeA
PGFAP
C1V1-mCherry
ITR
ITR
b
AstrOpto
λ542nm 3min
C1V1
CeL/C
CeM
IPSC
g
OTR-cKO mouse
AAV
CeA
PGFAP
GFP-IRES-Cre
ITR
ITR
c
IPSCs frequency (Hz)
Basal
AstrOpto
Wash
BAPTAstro
Basal
AstrOpto 542nm 3min
Wash
100 pA
2 s
d
IPSCs frequency (Hz)
Basal
TGOT
Wash
BAPTAstro
AP5
Basal
TGOT
TGOT + AP5
100 pA
2 s
f
IPSCs frequency (Hz)
WT
GFAP OTR KO
Basal
TGOT in WT
TGOT in GFAP OTR KO
100 pA
2 s

Figure 6

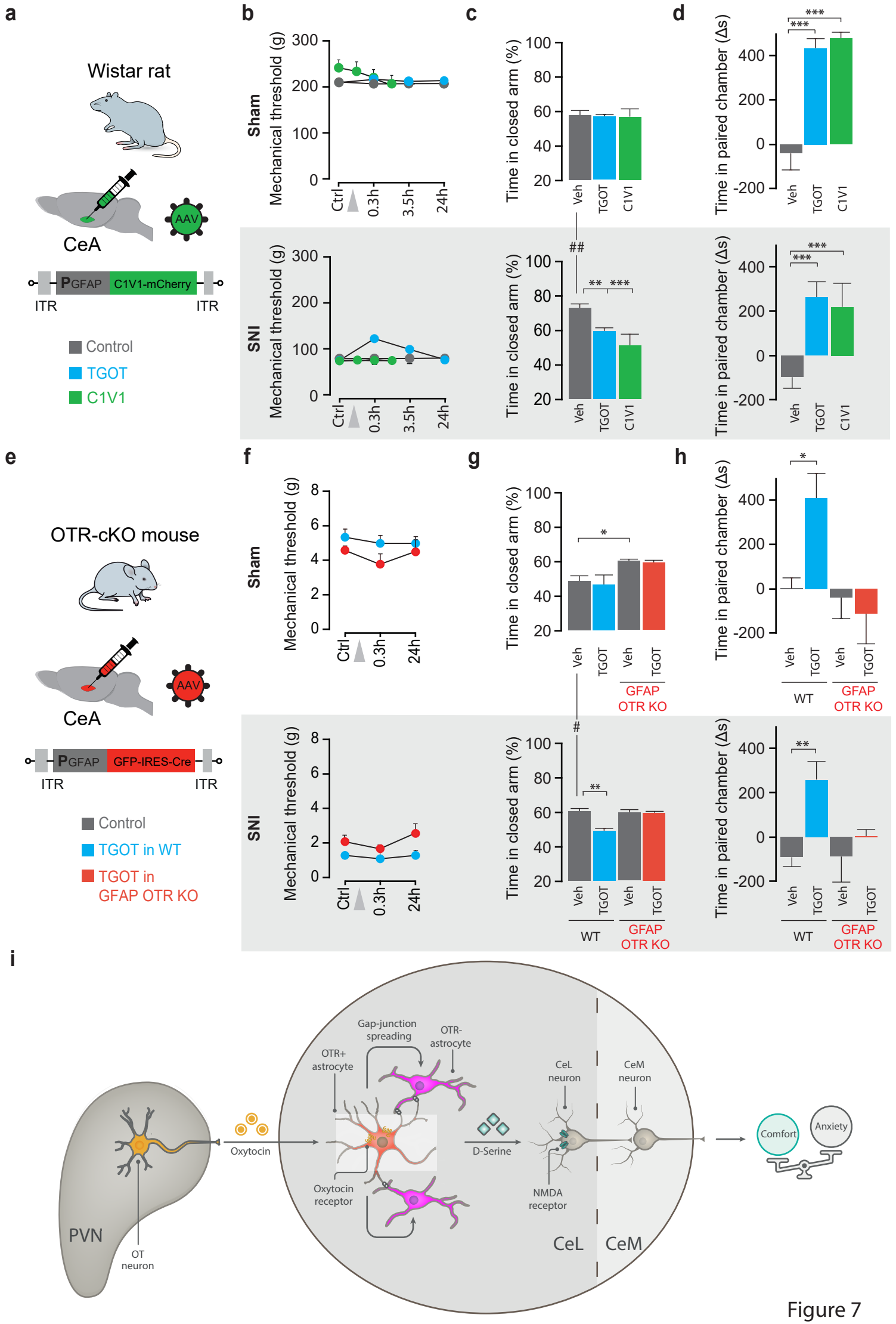
a
Wistar rat
AAV
CeA
PGFAP
C1V1-mCherry
ITR
ITR
Control
TGOT
C1V1
b
Sham
Mechanical threshold (g)
300
200
100
0
Ctrl
0.3h
3.5h
24h
SNI
c
Time in closed arm (%)
100
80
60
40
20
Veh
TGOT
C1V1
##
**
***
d
Time in paired chamber (Δs)
400
200
0
-200
***
e
OTR-cKO mouse
AAV
CeA
PGFAP
GFP-IRES-Cre
ITR
ITR
Control
TGOT in WT
TGOT in
GFAP OTR KO
f
Mechanical threshold (g)
8
6
4
2
0
Ctrl
0.3h
24h
g
Time in closed arm (%)
Veh
TGOT
Veh
TGOT
GFAP
OTR KO
#
**
*
h
Time in paired chamber (Δs)
WT
GFAP
OTR KO
i
PVN
OT
neuron
Oxytocin
Gap-junction
spreading
OTR-
astrocyte
OTR+
astrocyte
Oxytocin
receptor
D-Serine
CeL
neuron
CeM
neuron
NMDA
receptor
CeL
CeM
Comfort
Anxiety

Figure 7

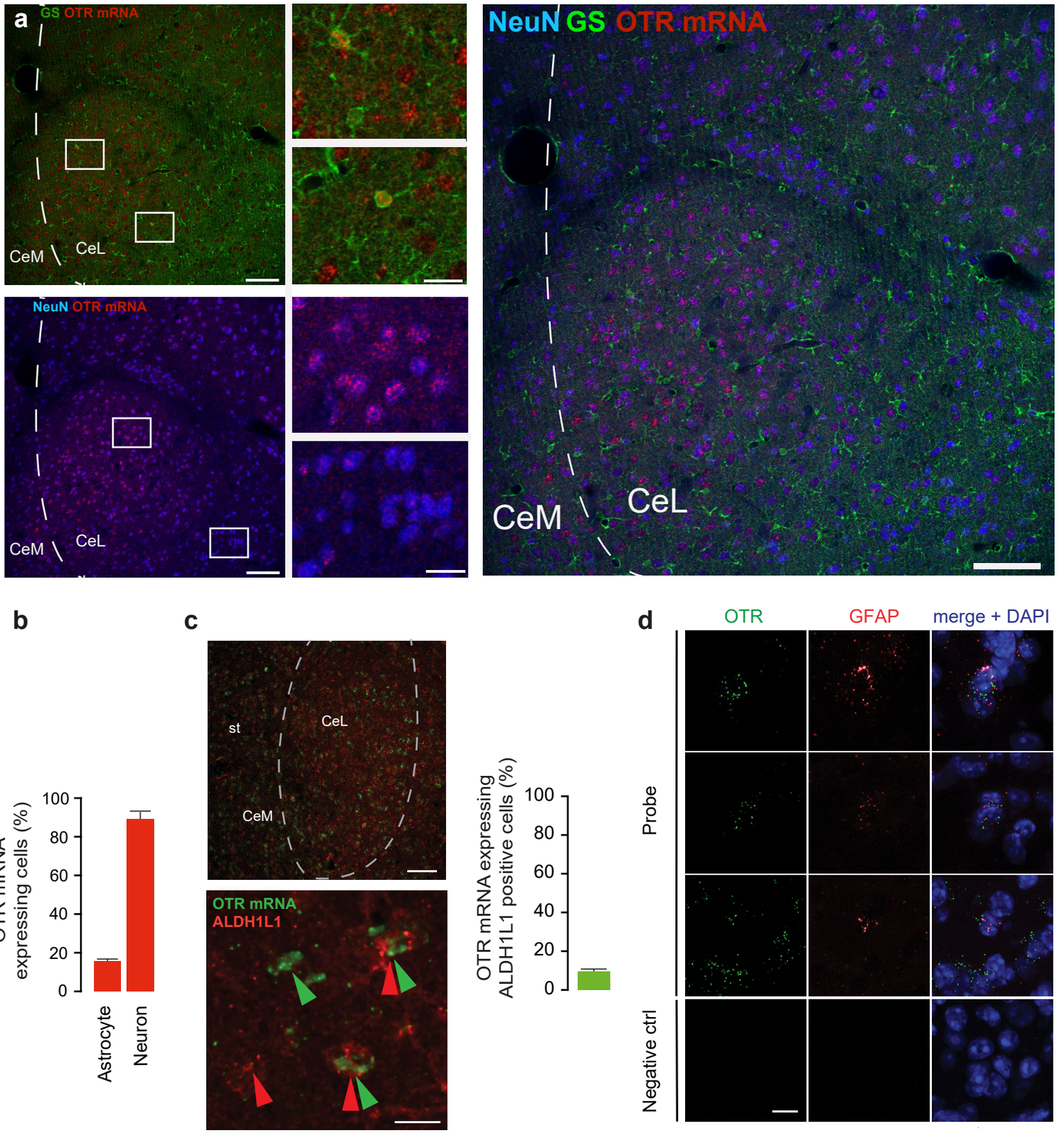

Extended Data Figure 1

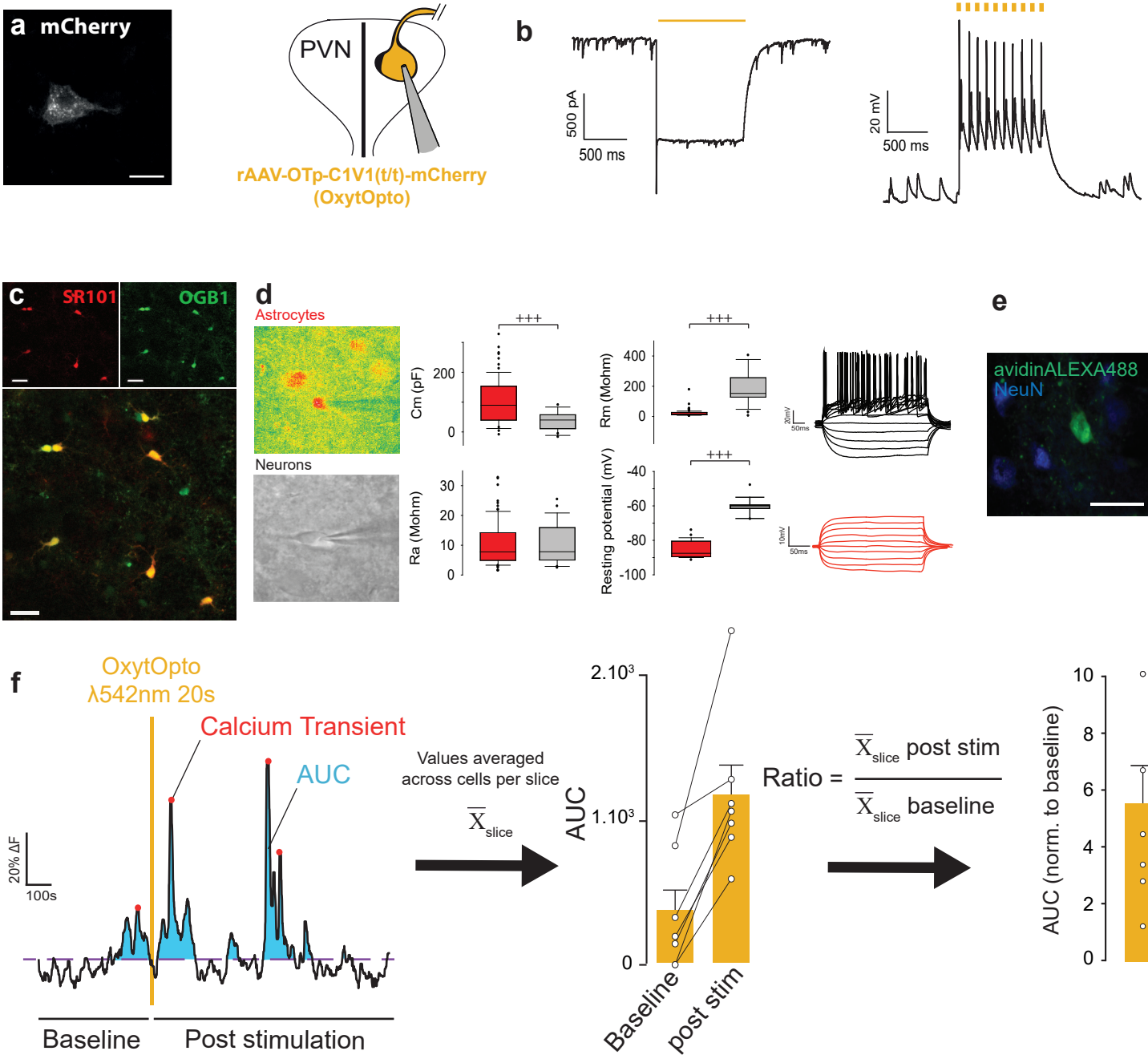

Extended Data Figure 2

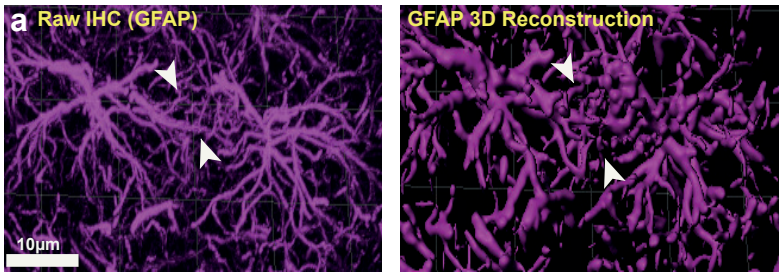

$$\text{Number of contacts} = \sum_{i=1}^{n} X_i$$

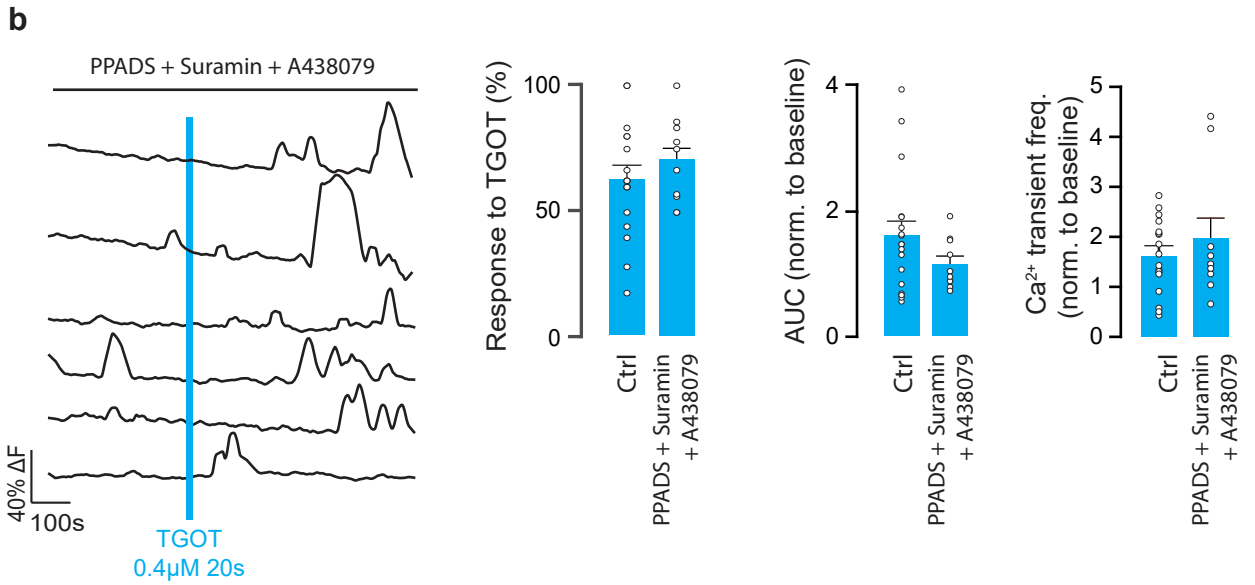

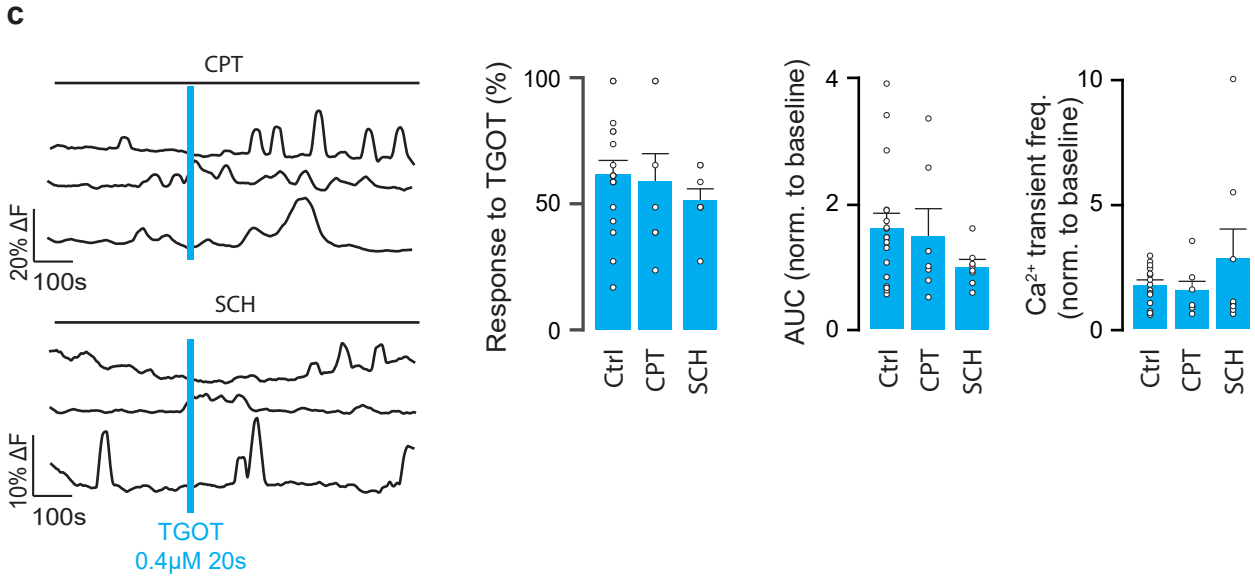

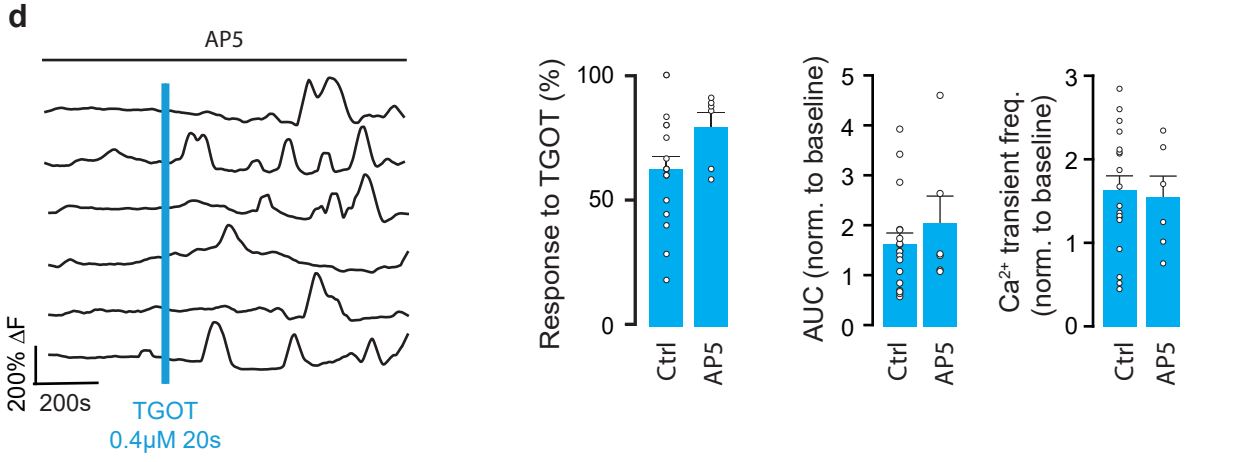

Extended Data Figure 3

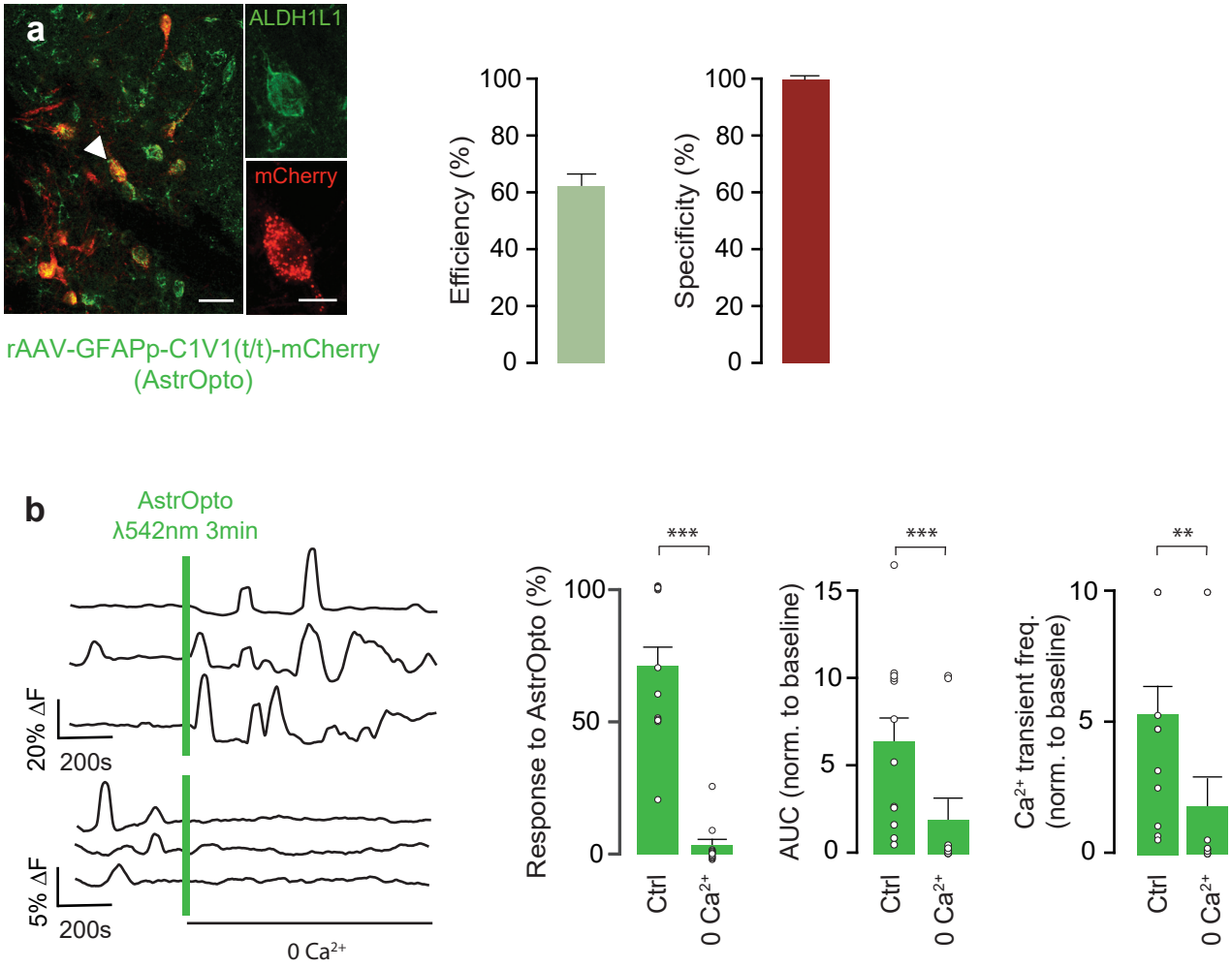

Extended Data Figure 4

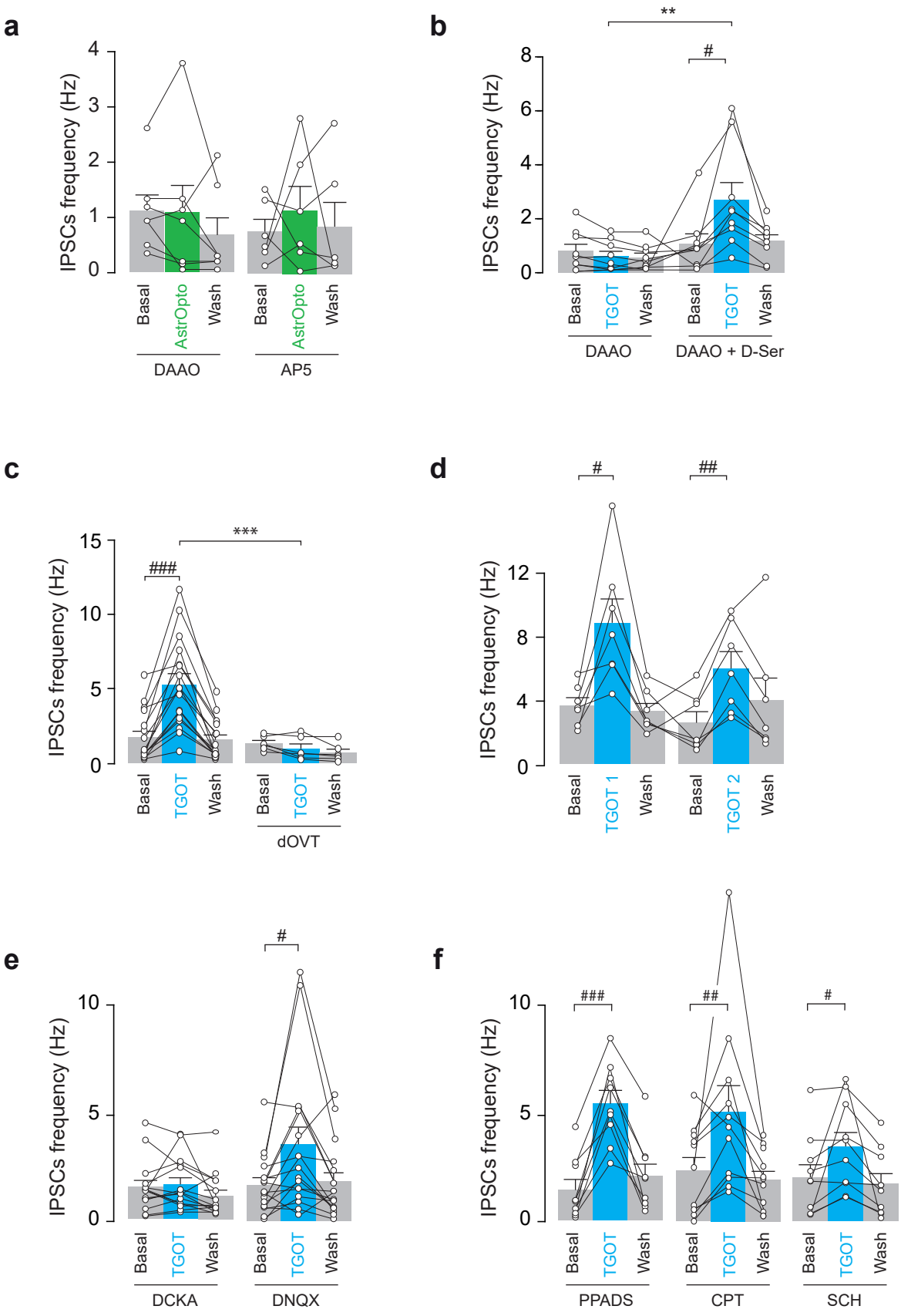

Extended Data Figure 5

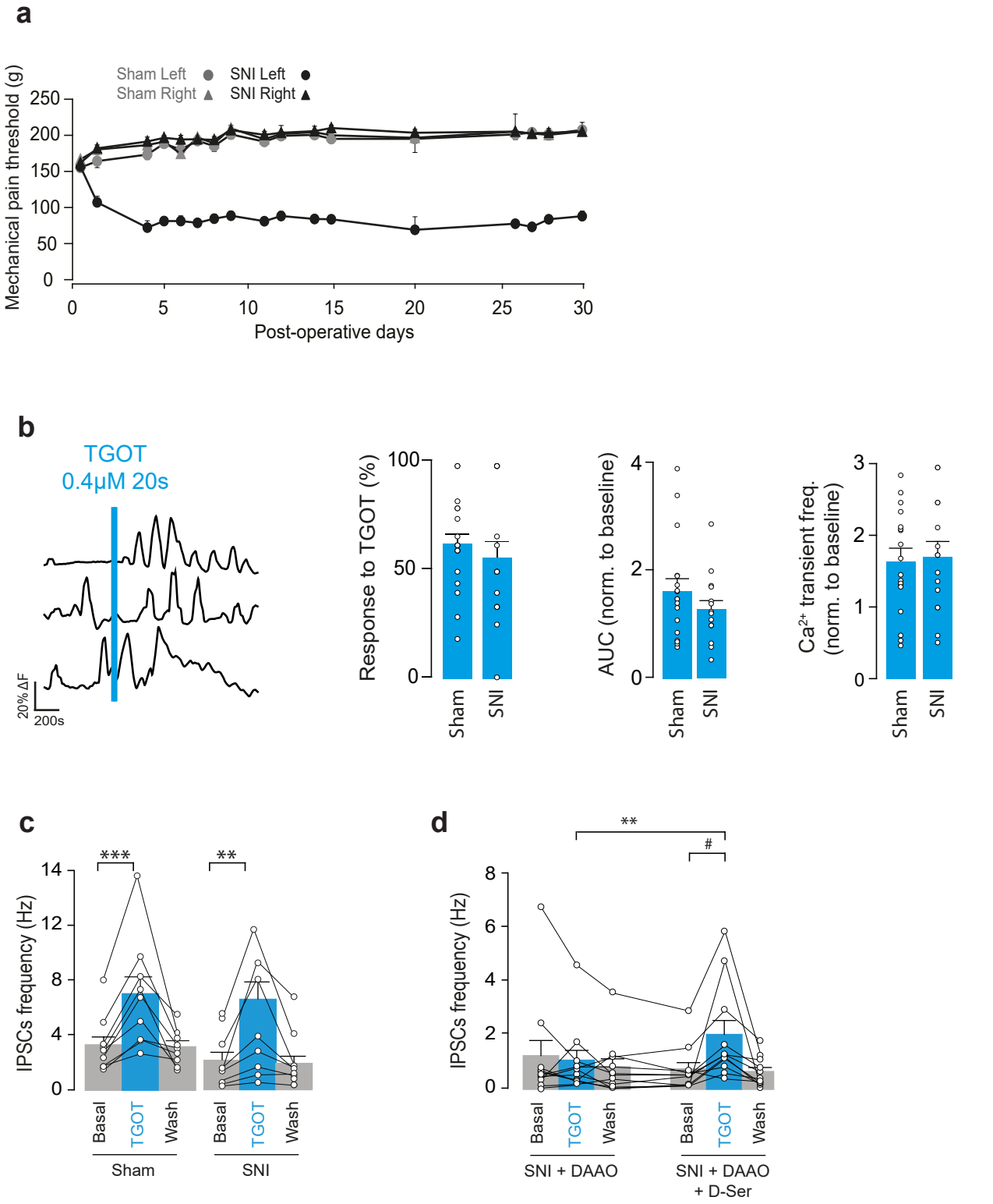

Extended Data Figure 6

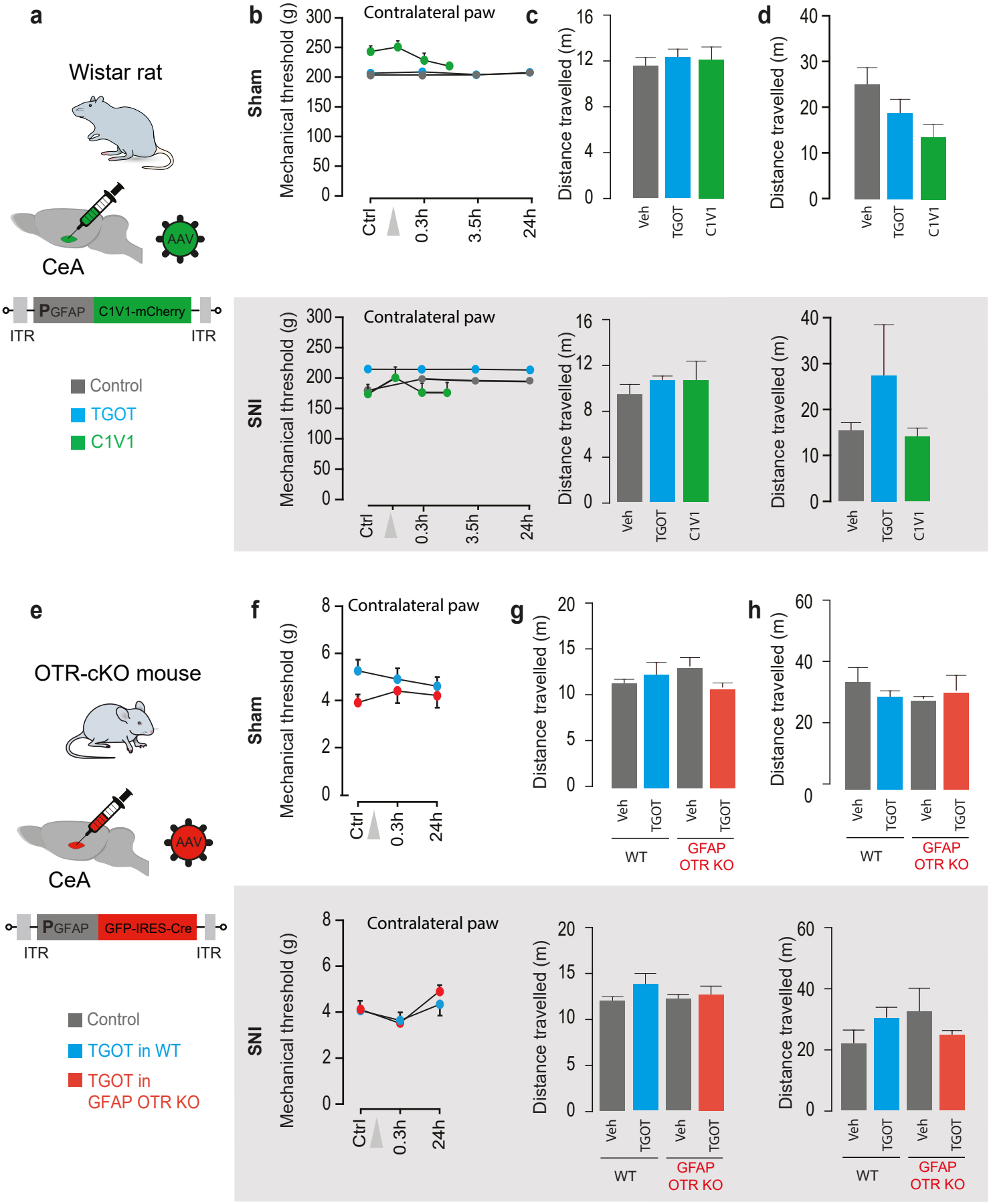

Extended Data Figure 7